Astron. Astrophys. 285, 833–856 (1994)

ASTRONOMY AND ASTROPHYSICS

Atomic hydrogen in the NGC 4631 group of galaxies

Richard J. Rand[1,2]

[1] Kapteyn Astronomical Institute, University of Groningen, Postbus 800, 9700 AV Groningen, The Netherlands
[2] Astronomy Department, University of Maryland, College Park, MD 20742, USA

Received 29 July 1993 / Accepted 18 October 1993

Abstract. We present WSRT observations of 21-cm line emission from the disturbed, edge-on galaxy NGC 4631. Maps at resolutions $12'' \times 22''$, $35''$, and $45'' \times 89''$ are presented, and these are used in conjunction with position-velocity cuts through the various data cubes in order to understand the structure of the disk and the many tidal spurs which protrude from this interacting galaxy. We also study the two companions NGC 4656 and NGC 4627, and three dwarfs in the system with H I detections.

We first attempt to get a rough idea of the structure of the disk of NGC 4631. The data can be well modelled by a differentially rotating disk with a steep fall-off beyond 4 kpc, and an outer disk restricted to the radius range 7–15 kpc. The latter component could simply be a set of spiral arms. Radial motions are probably present in the central few arcminutes. The inner disk bends upwards with increasing distance from the center on both the east and west sides. Strong tides may be responsible.

The H I layer at high resolution shows many disturbances, a large extent parallel to the minor axis, and a ragged appearance along its edges. The velocity structure of the gas far from the major axis of NGC 4631 suggests that most of this emission is due to the galaxy being not quite edge-on, a rather large (500–1000 pc) scale-height in the outer galaxy, and the connection of one of the spurs with the disk. A few high latitude features with a probable inner disk origin are found, and these are more likely to be due to gas raised out of the plane by stellar winds and supernovae. However, outer galaxy star formation may contribute to the large H I scale-height there.

No gas can be unambiguously associated with the dwarf elliptical companion, NGC 4627. It is difficult to identify any of the spurs as gas that once belonged to this galaxy (despite recent signs of star formation), as in the model of Combes. Modelling of the tidal encounters should now be redone, since more tidal debris has been discovered and an optical velocity of NGC 4627 has been determined.

Position-velocity diagrams parallel to the major axis of the edge-on companion, NGC 4656, reveal a ring-like structure in the inner 15 kpc. Furthermore, the high and low-velocity sides of the ring arise from opposite sides of the midplane. Two possible explanations are given for this structure. First, NGC 4656 may consist primarily of two loosely wrapped tidal arms, viewed not quite edge-on. Second, NGC 4656 may be a ring galaxy similar to the Cartwheel. The south-west side of the disk shows many "worms" (or vertical filaments) with velocities consistent with an outer disk origin. The most prominent worm, however, is on the north-east side, above the center of the major axis. Its mass is $\sim 3 \times 10^7 M_\odot$. At very marginal signal-to-noise ratios, the worm bends around to form a complete loop.

Key words: Radio lines: galaxies – galaxies indiv: (NGC 4631, NGC 4656, NGC 4627) – galaxies: ISM – galaxies: interactions – galaxies: kinematics and dynamics

1. Introduction

Not many galaxies are better suited for a study of the effects of galactic interactions on the vertical structure of gas disks than the nearby, nearly edge-on Sc galaxy NGC 4631. This galaxy has two prominent companions: a dwarf eliptical, NGC 4627, at about 3′ NW of the nucleus, and another edge-on spiral, NGC 4656, at about 30′ to the SE. The main properties of NGC 4631 are summarized in Table 1. Previous Westerbork Synthesis Radio Telescope (WSRT) observations (Weliachew et al. 1978; hereafter WSG) at a resolution of $48'' \times 89''$ revealed a complex distribution of H I emission, with four long spurs of H I protruding out of the warped main gas layer of the galaxy. Other recent observations of NGC 4631 are relevant for understanding how this galaxy has been disturbed. Hα observations by Rand et al. (1992; hereafter RKH) revealed a bright, thick, disturbed disk of ionized gas with much structure, patchy emission, a few loops up to 1.5 kpc from the plane, and a "double-worm" [a closely-spaced pair of nearly vertical filaments; throughout the text we make frequent use of the term "worm" to refer to vertical gas filaments in analogue to the Galactic worms studied by Heiles (1984)] standing above the nuclear region. This latter feature is probably a blown-out superbubble from a nuclear starburst. NGC 4631 has a very extended radio halo, featuring several spurs, which is probably due to convection of cosmic rays upwards from the disk (Hummel & Dettmar 1990). Recent

Send offprint requests to: R.J. Rand (Univ. of Maryland)

ROSAT observations have revealed a similarly impressive X-ray halo (Walterbos 1993). These results suggest a scenario in which the interaction has caused the strong star formation activity, which in turn may be responsible for the extended X-ray and radio halos due to upward convection of hot gas and cosmic rays produced in the disk.

This suggested active disk-halo cycling of gas should have consequences for the structure of the H I layer. We have therefore mapped the NGC 4631 system at the full resolution ($12'' \times 22''$) of the WSRT. The first results from this study have already been reported by Rand & van der Hulst (1993; hereafter RH). RH focussed on the discovery of two large "supershells" in the disk, which have diameters of 3 and 1.8 kpc, and appear to be expanding at velocities of 50 and 35 km s^{-1}, respectively. If the expansion is real, then the energy required to power these shells is so enormous that the standard explanation for the formation of such shells, namely multiple stellar winds and supernovae, becomes difficult to accept. An alternative explanation is that external objects collided with the disk and formed the shells as a consequence. The discovery of a new tidal feature and H I emission in two more dwarfs in the NGC 4631 system was also reported by RH.

The first goal of this paper is to present the basic data. We win then discuss the structure of the main H I disk of NGC 4631. Our next goal is to understand the nature and origin of gas far from the plane. To what degree is it an inclination effect? Are high-z worms or shells of H I prevalent? Is this emission mostly due to gas raised out of the plane by star formation or gravitational effects such as tides, warping or flaring? We also search for gas associated with NGC 4627. The main disk and emission off the plane of the edge-on companion, NGC 4656, is also studied, with the same issues in mind. Finally, the properties of the smaller dwarfs are summarized. As tools for answering these questions, channel maps at various resolutions are presented, and extensive use is made of position-velocity diagrams, especially ones parallel and perpendicular to the disks of NGC 4631 and NGC 4656.

Following Hummel et al. (1984), we adopt a distance of 7.5 Mpc to the NGC 4631 group, based on $H_0 = 100\,\mathrm{km\,s^{-1}}$ kpc^{-1}. It should be noted that WSG used a smaller value of 5.2 Mpc when comparing the current results to theirs.

2. Observations

The observations were made with the WSRT between April and November 1991. See Table 2 for details. After standard Westerbork calibration, the data were Fourier transformed both with and without a Gaussian taper to produce dirty maps at $45'' \times 87''$ and $12'' \times 22''$ resolution. The former resolution was chosen to match that of the previous WSRT observations by WSG. Further processing was carried out with the new Unix-based GIPSY package (van der Hulst et al. 1992). Continuum subtraction was achieved by performing a pixel-by-pixel linear fit to the spectrum in two sets of ten line-emission free channels at either end of the velocity axis. To clean the maps, a rough clean of the two sets of dirty maps was first carried out, and the resulting cubes were then used to define the search areas for the clean components on a channel-by-channel basis for deeper cleans. During the analysis it became obvious that intermediate resolution cubes were necessary to address some issues, so $35''$ and $50''$ cubes were produced by smoothing the full-resolution cube with a Gaussian. The channel width is 8.28 km s^{-1} and a uniform taper was applied which resulted in a velocity resolution of 10 km s^{-1}. Our 5σ detection limit in the full-resolution cleaned cube for a point source at the pointing center fully contained in one channel is $7 \times 10^5 M_\odot$. In all the figures shown, no primary beam correction has been applied.

Zeroth and first moment maps at each resolution were produced by the so-called conditional transfer method (e.g. Bosma 1981) in an attempt to salvage as much signal and eliminate as much noise as possible. The original cleaned cube was smoothed in the spatial dimensions by a factor of three. Then the original cube was blanked wherever the smoothed cube did not exceed three times its noise level. Moment maps were then made using only data which at each pixel exceeded 1–1.5 times the noise level in two or more consecutive channels. The resulting maps bring out more real diffuse, low-level emission than those shown in RH. Note that a first moment map for an edge-on galaxy is not a velocity field in the usual sense because of the large spread in observed velocities of gas along each line of sight.

3. Results

3.1. General properties

Channel maps are presented in Figs. 1–3 at resolutions of $45'' \times 87''$, $35''$, and $12'' \times 22''$ respectively, for the velocity range V_{hel} = 435–782 km s^{-1}. Maps of total intensity at these resolutions are shown in Figs. 4 (overlaid on optical images of NGC 4631 and NGC 4656), 5 (overlaid on the Hα image of RKH), and 6. First moment maps at $45'' \times 87''$ and $12'' \times 22''$ resolution are shown in Figs. 7 and 8, respectively. The main features of the NGC 4631 system can be clearly seen in these figures: the main disk of NGC 4631, the disk of the edge-on companion, NGC 4656, and the four spurs first reported by WSG. The bottom half of the larger of the two supershells discussed by RH (Shell 1) is visible in the high-resolution map of total intensity, near the eastern end of the disk (the top half of Shell 1 and all of Shell 2 are not visible because of confusion from other emission along the lines of sight toward them). This map also shows the layer to be quite disturbed, with a ragged appearance to its edges which is not due to noise. The new spur reported by RH (Spur 5) is also labelled in Fig. 4, as are the newly-detected dwarfs. Since RH was published, H I emission from a third dwarf has been discovered in the system, which is also labelled in Fig. 4. Note that NGC 4656 is well outside the half-power points of the primary beam. The relative response of the primary beam at its location is about 15%. Table 3 gives a summary of the main properties of the H I features in the system.

Table 1. Parameters and properties NGC 4631

		Reference
Type	Sc	Sandage (1961)
Assumed distance	7.5 Mpc	Hummel, Sancisi, & Ekers (1984)
Adopted position of center (1950.0)	R. A. $12^h39^m41.2^s$ Dec. 32°48′56.2″	Ekers & Sancisi (1977)
Inclination	85°	Hummel & Dettmar (1990)
Position Angle of Major Axis	86°	This work; WSG
Heliocentric Systemic Velocity	610 km sec^{-1}	This work; WSG
Rotation speed	150 km sec^{-1}	This work;WSG
Hα luminosity[a]	1.6×10^{41} erg s^{-1}	Rand, Kulkarni & Hester (1992)
1.5 GHz flux density	22 mJy	Hummel & Dettmar (1990)
FIR luminosity	9×10^9 $L_\odot$	Rice et al. (1988)

[a] Corrected for Galactic extinction.

Table 2. Parameters of the observations

Period of the observations	April–November 1991
Number of 12-hour tracks	8
Number of interferometers	40
Range of baseline lengths	36–2736 m
Radius of first grating ring	40′ × 75′
FWHM of synthesized beam	11.5″ × 21.5″
Channel width	8.28 km s^{-1}
Velocity resolution	10 km s^{-1}
Range of V_{hel} covered	112–1023 km s^{-1}
FWHM of primary beam	37.5′
r.m.s. noise in channel maps	2.8 K
Conversion factor $T_B(K)/S$(mJy/beam area) at 11.5″x21.5″ resolution	2.4

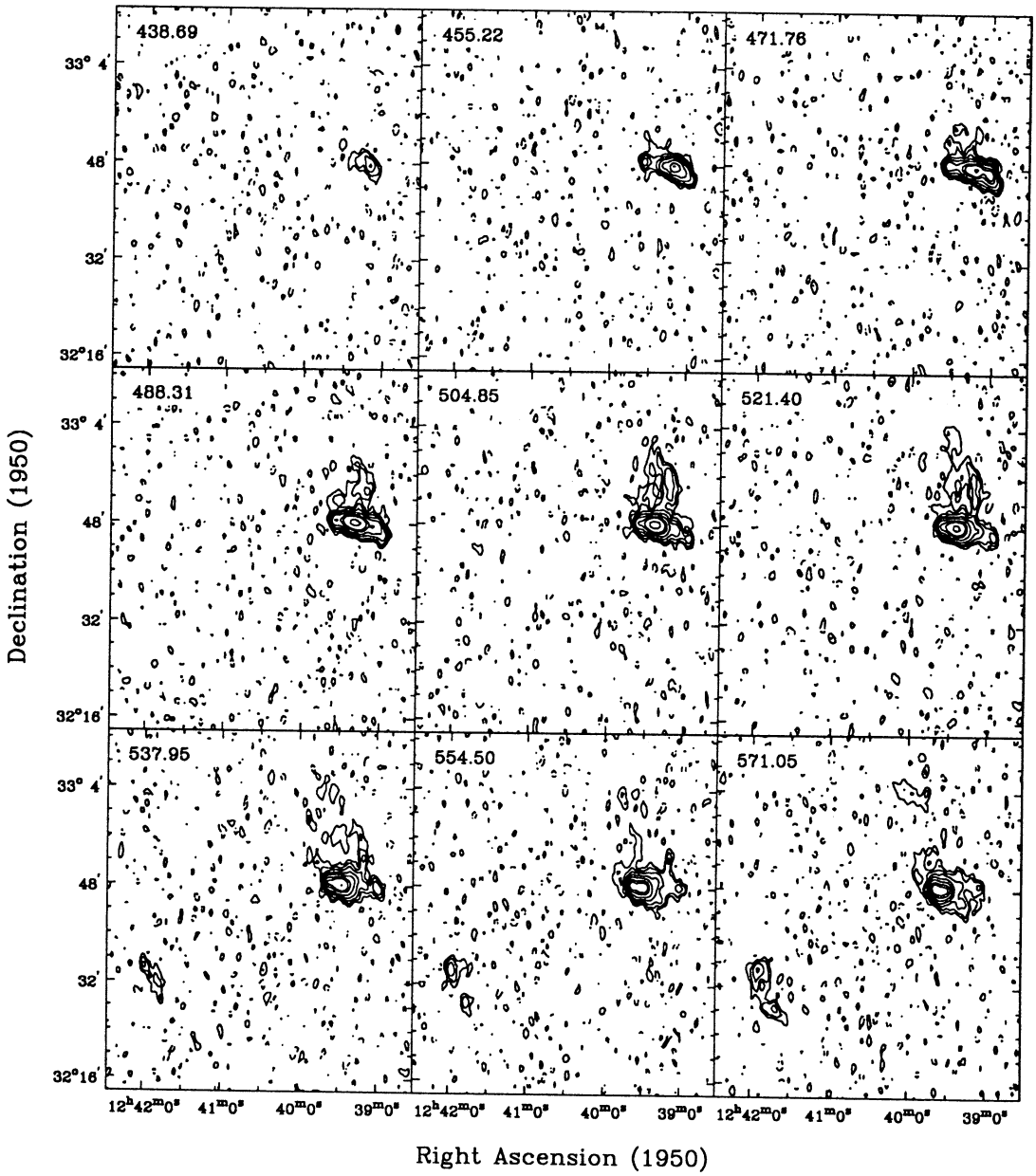

Fig. 1. Channel maps of the NGC 4631 system at 45″ × 87″ resolution. Pairs of channels have been summed together, and the mean velocity of the two channels is indicated in each panel. The contour levels are −4, −2, 2, 4, 6, 8, 16, 32, 48, and 96 times the noise in a summed pair of channel maps of 0.4 K. No primary beam correction has been applied

3.2. Structure of the main H I disk of NGC 4631

Being a disturbed, nearly edge-on galaxy, NGC 4631 is not ideal for a study of disk structure of the nature of spiral arms or bars, for example. Hence, we do not present any rigorous modelling of the disk here, but use several views of the data and a few models to draw some simple conclusions.

Figure 6, the full-resolution map, shows only relatively weak emission from the tidal spurs, which have been largely resolved out, but best reveals the disk structure. The main disk shows the following features. First, there is a concentration in the inner 2–3′. The layer is strongly pinched on the east side at 2′ radius (in Hα emission too; see Fig. 5), and beyond this radius the layer broadens again and the bottom half of Shell 1 can be seen. On the west side, there is another concentration at 3–5′ from the center, just westward from Shell 2. (As an aside, we note that radio continuum emission at 1.5, 2.7, and 3.6 GHz (Duric et al. 1982; Hummel & Dettmar 1990; Hummel, pers. comm.) shows a bright concentration in the central 3′ and features further from the center coincident with Shell 1 and the western H I concentration.) At the eastern and western ends of the major axis, the layer bends upward and downward, respectively. This is either due to a global warp or local tidal disturbances which have pulled Spurs 1 and 4 out of the disk (see Sect. 3.3). The entire layer is generally more extended on the south side.

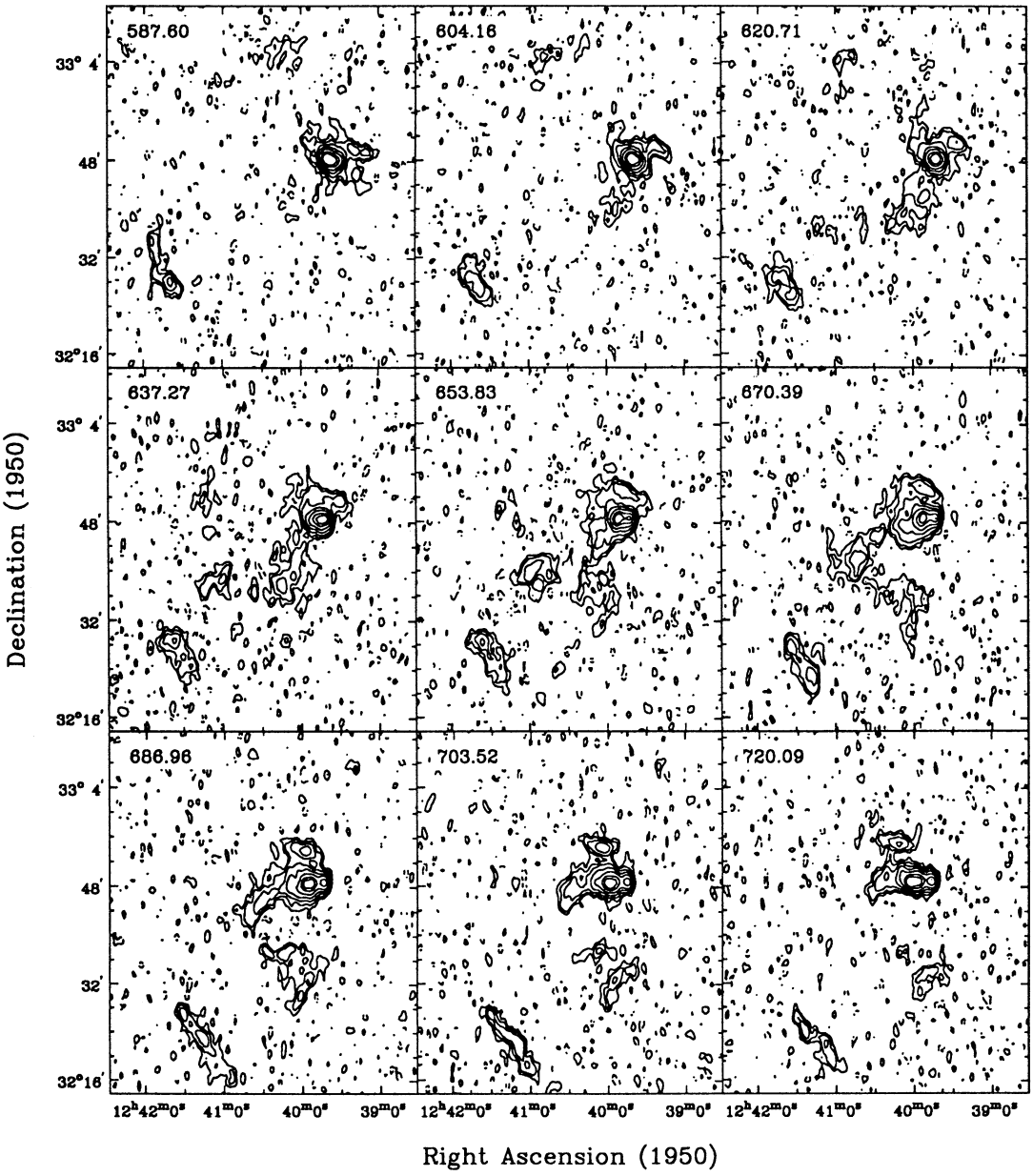

Fig. 1. (continued)

Rather than discussing further the velocity contours in Fig. 6 and the vertical structure of the emission at this point, we turn to position-velocity diagrams parallel to the major axis ($l - v$ diagrams) from the full-resolution cube, which best reveal the kinematic components of the main disk (Fig. 9). Some of these were first shown in RH to demonstrate the kinematic structure of the supershells. These diagrams will also often be referred to in subsequent sections as an aid in relating the observed velocities of emission features to their probable locations along the line of sight, under the assumption of circular rotation.

The midplane cut reveals the basic kinematic structure of the disk and suggests differential rotation but with a density enhancement in the outer parts. Therefore, to understand the disk structure, we have attempted to model the emission in this figure with a differentially rotating disk and an outer ring, using the program GALMOD in the GIPSY package. In this program, uniformly rotating kinematic components with specified radial density profiles, rotation curves, dispersions, vertical distributions, inclinations and position angles can be used to create a model cube to compare with real data, after convolving to the beam size and smoothing to the velocity resolution. We only consider axisymmetric components. We will first compare midplane $l - v$ diagrams of the data and the best model and then discuss constraints on the vertical structure of the emission.

An exhaustive search of parameter space was felt not to be justified because the disturbances to NGC 4631 limit what we can infer about its axisymmetric properties. Mainly for completeness, the parameters of the best model are given in Ta-

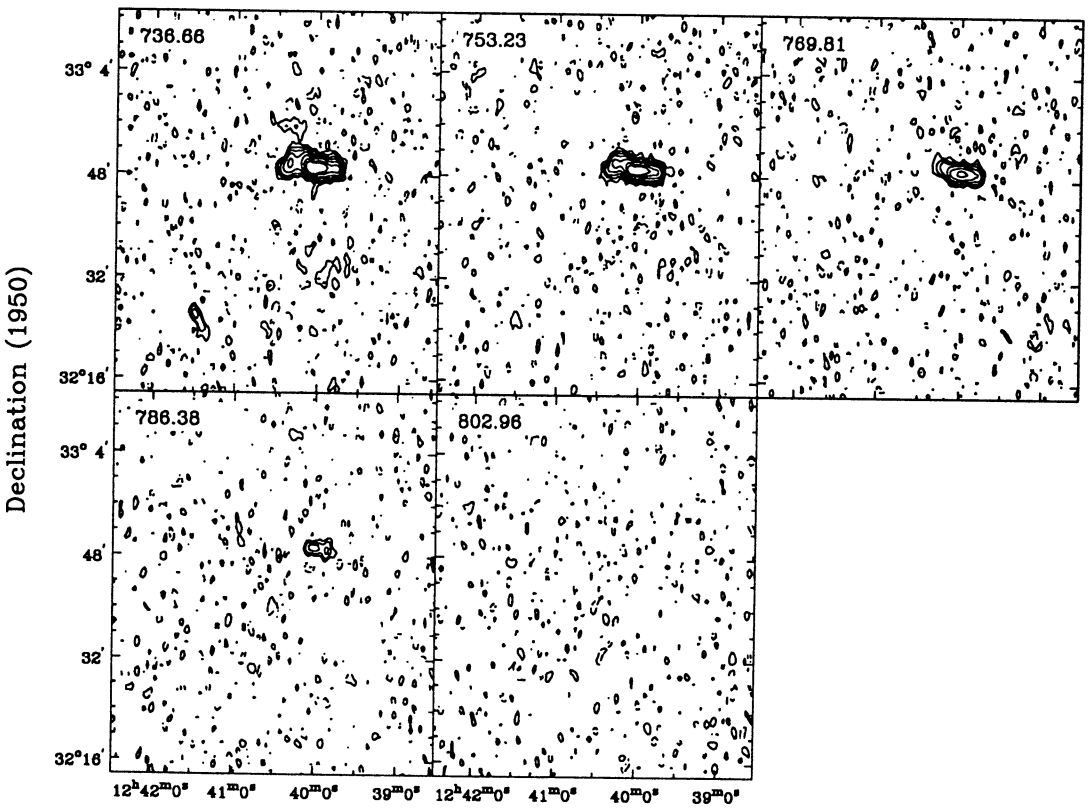

Fig. 1. (continued)

ble 4. The model density profile is shown in Fig. 10. The results of most significance from the modelling are discussed here. The model reproduces the midplane $l - v$ diagram reasonably well (Fig. 11). The inner, differentially rotating disk must have a rapid density falloff beyond $R = 4$ kpc to match the observations (hence we will refer to it as the "inner disk"). The broad, outer ring will be simply referred to as the "outer disk". On the east side, the intermediate radius where neither component is bright corresponds to the radius where the H I layer is pinched (Fig. 6). The density in the bright parts of both components is about 0.5 cm^{-3}. The outer disk fits the data much better if its systemic velocity is lower than that of the inner disk by $\sim$ 10 km s^{-1} , and if its rotation curve rises from 100 km s^{-1} to 140 km s^{-1} over the range R = 7–11 kpc and is flat thereafter (note that the disk rotation curve is flat where the outer component is rising, which is unphysical, but the disk rotation is not well constrained here because of its low contribution to the emission). The modelling suggests a velocity dispersion in the plane of 15 km s^{-1}. A dispersion of 10 km s^{-1} produces velocity profiles in the outer disk which are too narrow. Although 15 km s^{-1} is a rather high dispersion for a galactic disk of H I (cf. Kamphuis 1993), non-circular motions probably contribute (see below). The total modelled H I mass is $9.5 \times 10^9 M_\odot$, somewhat higher than the measured mass. The "outer disk" could be a real ring as in the model, but it may simply be reasonably tightly wrapped spiral arms, which would roughly mimic a ring in such $l - v$ diagrams.

Disturbances to the disk, such as the two shells (the systemic velocities of which suggest that they lie in the outer component), cause the data and model to disagree in detail (in fact, if the outer component initially had the symmetry around the major axis present in the model, then the deficiency of gas observed in the region of Shell 1 in Fig. 9 would provide further evidence that this region has been evacuated of gas). The very outer parts of the disk are also not well reproduced by the model, but disturbances due to the encounters are probably the reason. In the inner four arcminutes, the modelled velocity profiles are too sharply peaked compared to the observations. This is demonstrated by comparing profiles at the center of the major axis, for example (Fig. 12). The fluxes under these two profiles differ by only 12%. This discrepancy in shape could be due to a velocity dispersion higher than modelled, but the dispersion is reasonably well constrained by the steepness of the falloff in emission at the full rotation speed (V_{hel} = 480 and 740 km s^{-1}) along the major axis in Fig. 9. Increasing the velocity dispersion of the components to an unrealistic 30 km s^{-1} broadens the profiles to match the data better, but at the expense of making the falloff at the full rotation speed much too shallow. Creating a central hole also does not solve the problem: the velocity profiles remain too sharply peaked and the inner, elongated contours in Fig. 11 begin to form a larger angle with the vertical than in the original model or the data. Self-absorption could flatten the tops of profiles and increase the FWHM somewhat, but it is unlikely that profiles as broad as those observed could be produced in this way. A likely explanation is that there are non-circular mo-

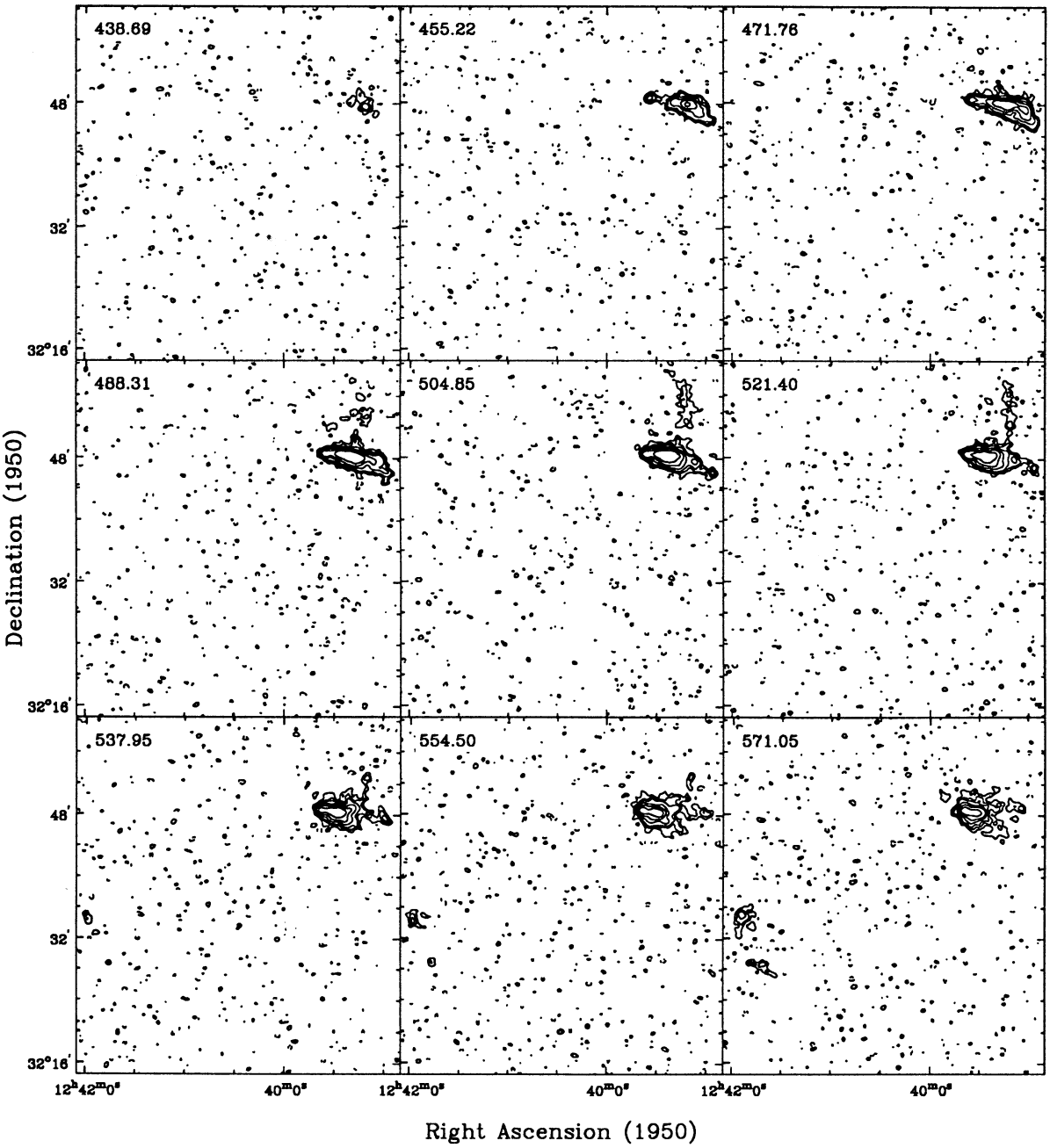

Fig. 2. Channel maps of the NGC 4631 system at 35″ resolution. Pairs of channels have been summed together, and the mean velocity of the two channels is indicated in each panel. The contour levels are −4, −2, 2, 4, 8, 16, 32, and 48 times the noise in a summed pair of channel maps of 1.0 K. No primary beam correction has been applied

tions in the inner disk or the outer component. These may be due to elliptical orbits or spiral structure, but may also be due to a general radial outflow or inflow.

We now turn to the vertical structure of the disk, using both data and the model. From Fig. 9, $l - v$ diagrams for emission above and below the plane show that the outer galaxy can be detected further from the major axis than the inner disk. The apparent warp perpendicular to the line of sight, evident in Fig. 6, can also clearly be seen in these figures: on the north side, the eastern half of the emission is brighter than the western half, while the opposite is true on the south side. The connection of Spur 2 onto the southern half of the galaxy (see below) also increases the vertical extent of the outer galaxy.

Further clues as to the disk structure are provided by position-velocity diagrams perpendicular to the major axis ($b-v$ diagrams). These are shown for most of the length of the major axis in Fig. 13. To improve the signal-to-noise ratio for extended emission, the data were averaged over three pixels along the major axis. For most of the plots on the east side of the galaxy (offsets −0.26 to −4.48), two main emission features can be seen.

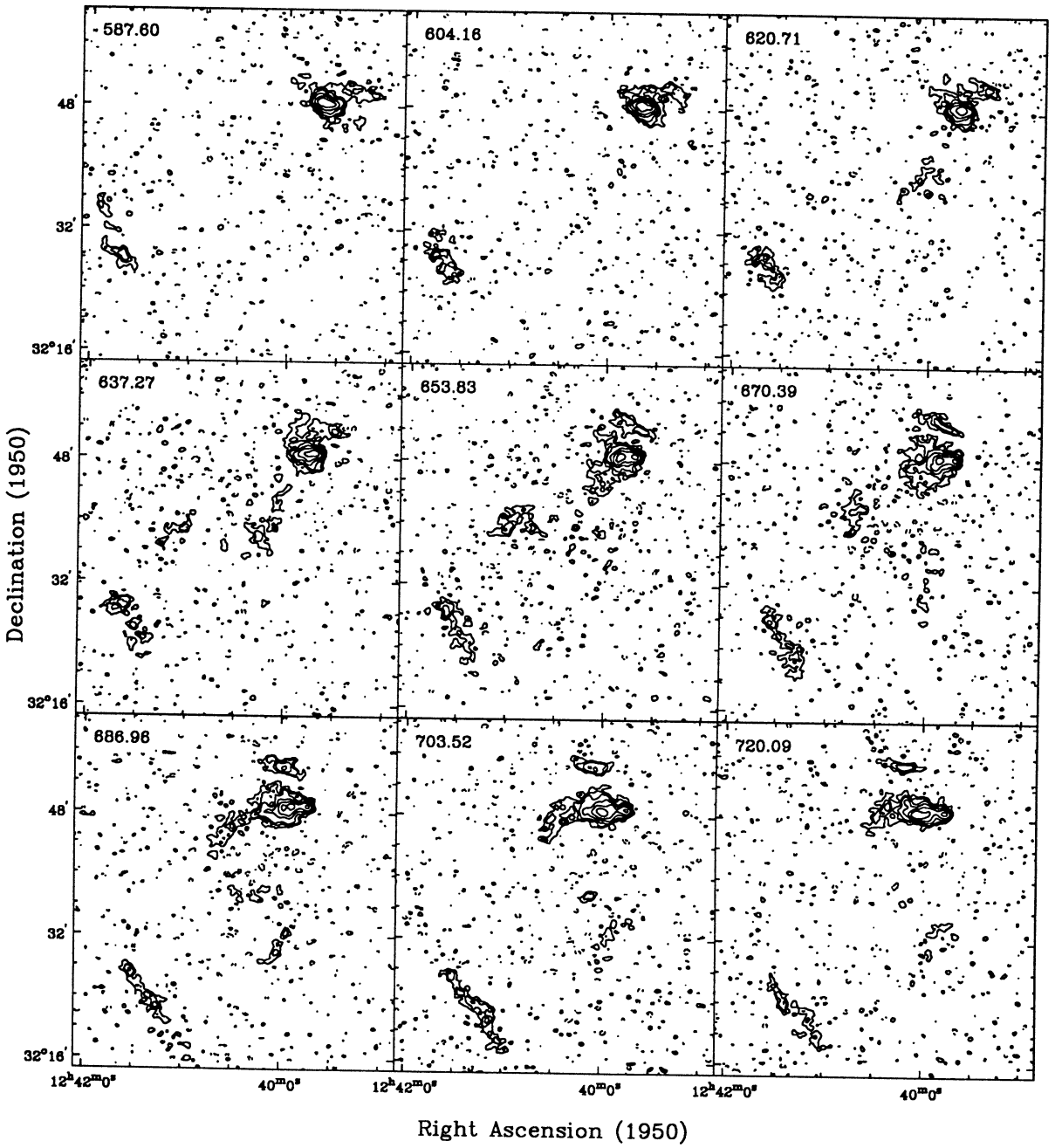

Fig. 2. (continued)

Comparison with the midplane $l-v$ diagram of Fig. 9 shows that the feature at higher $V_{\rm hel}$ is associated with the inner disk, while the one at lower $V_{\rm hel}$ corresponds to the outer component. On this side, the outer component lies exactly on the adopted major axis except in the region of Shell 1 (offsets -2.61 to -4.22), where it is displaced to the south. Also on the east side, the inner disk bends upwards with distance from the center, eventually reaching about 35″ or 1.3 kpc above the adopted midplane. On the west side, the emission does not divide as nicely into two components, but in the inner 3′ or 6.5 kpc, the emission with the lowest $V_{\rm hel}$, which is from the inner disk, rises slightly above the major axis. The outer component, which is seen at higher values of $V_{\rm hel}$ in the inner 3′ and dominates the emission beyond this radius, shows no displacement from the midplane until about radius 6′ or 13 kpc, where it begins to bend downward slightly. A bend in the inner disk of a galaxy is unusual and we suggest that strong tidal interactions are responsible.

The larger extent of the outer galaxy parallel to the minor axis is expected if the inclination is less than 90°. In the model, the combination of the inclination and scale-height of the components is subject to several constraints. The model must first reproduce reasonably well the midplane $l-v$ diagram and the zeroth moment map. Models with $i \geq 88°$ predict too much emission from the outer disk in the inner 4′ for any scaleheight

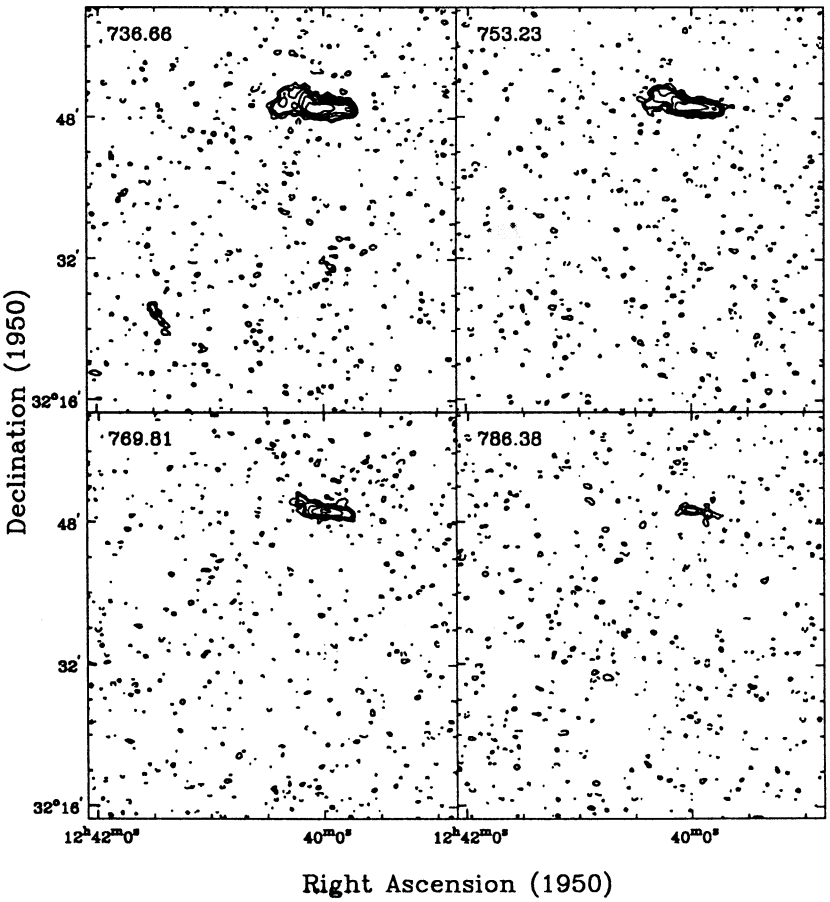

Fig. 2. (continued)

which produces a reasonable match to the minor axis emission profile in the zeroth moment map). The vertical structure is also constrained by $b - v$ diagrams, especially at radii where the inner and outer disks are well separated in velocity. Finally, channel maps must be reasonably well produced. In particular, the outer disk must not be seen to split into two components parallel to the minor axis corresponding to the near and far sides seen in projection. For $i \leq 83°$, this can be avoided by choosing large scale-heights, but then the modelled zeroth moment map becomes too extended along the minor axis. In this way, the inclination is constrained to be 84–87°, the scale-height of the outer disk is roughly 500–1000 pc, and that of the inner disk is 400–600 pc. More accurate values are difficult to obtain given the disturbances in the gas layer. It is difficult to rule out the possibility that part of the large z-extent in the outer galaxy could be due to a warp along the line of sight.

The total column density and first moment maps for the best model, and for each of the components separately, are shown in Fig. 14. While the model does only a fair job of reproducing Fig. 6, the comparison confirms the trends found above for the vertical structure of each component. The deformation of the 525 km s^{-1} contour of the observed first moment map is due to Shell 2, most of which emits at relatively high values of $V_{\rm hel}$ for its location. The pinching at the ends of the modelled disk are simply an artifact of the boundary conditions; we did not try to reproduce the observed shape at these locations.

3.3. The tidal spurs

In this section we discuss the structure of the many tidal spurs emanating from NGC 4631, with particular attention to how and where they join onto the main disk. The five main spurs are labelled in Fig. 4.

Although emission from the spurs is mostly resolved out in the full-resolution channel maps, they do show well how Spur 1 joins onto the disk. Tracing Spur 1 as it moves to the northwest with increasing $V_{\rm hel}$ in Fig. 3, it can be seen that the spur bifurcates before it reaches NGC 4631, and joins onto the disk at two locations and velocities. Firstly, over the range $V_{\rm hel}$ = 666–699 km s^{-1}, it appears as a patchy region joining onto the lower half of the disk near Shell 1. Secondly, over the range $V_{\rm hel}$ = 732–766 km s^{-1}, it can be traced further northwards, rising above the major axis of the disk and forming a bridge with the disk, which also bends sharply upwards, in the 749 km s^{-1} channel. This sharp bend in the main disk is clearly visible in the integrated H I map of Fig. 6. At the southeast end, Spur 1 does not reach NGC 4656 in maps of any resolution, even when the data are smoothed to a resolution of 3′. The projected length of Spur 1 is about 60 kpc.

Spur 2 has a much more complex structure. RH pointed out that Spur 2 connects onto the main disk over a large section of the major axis east of the nucleus (Fig. 5). However, the 45″ × 87″ channel maps show that the connection region even extends to the western side, as far as R.A. = 12$^{\rm h}$39$^{\rm m}$30$^{\rm s}$

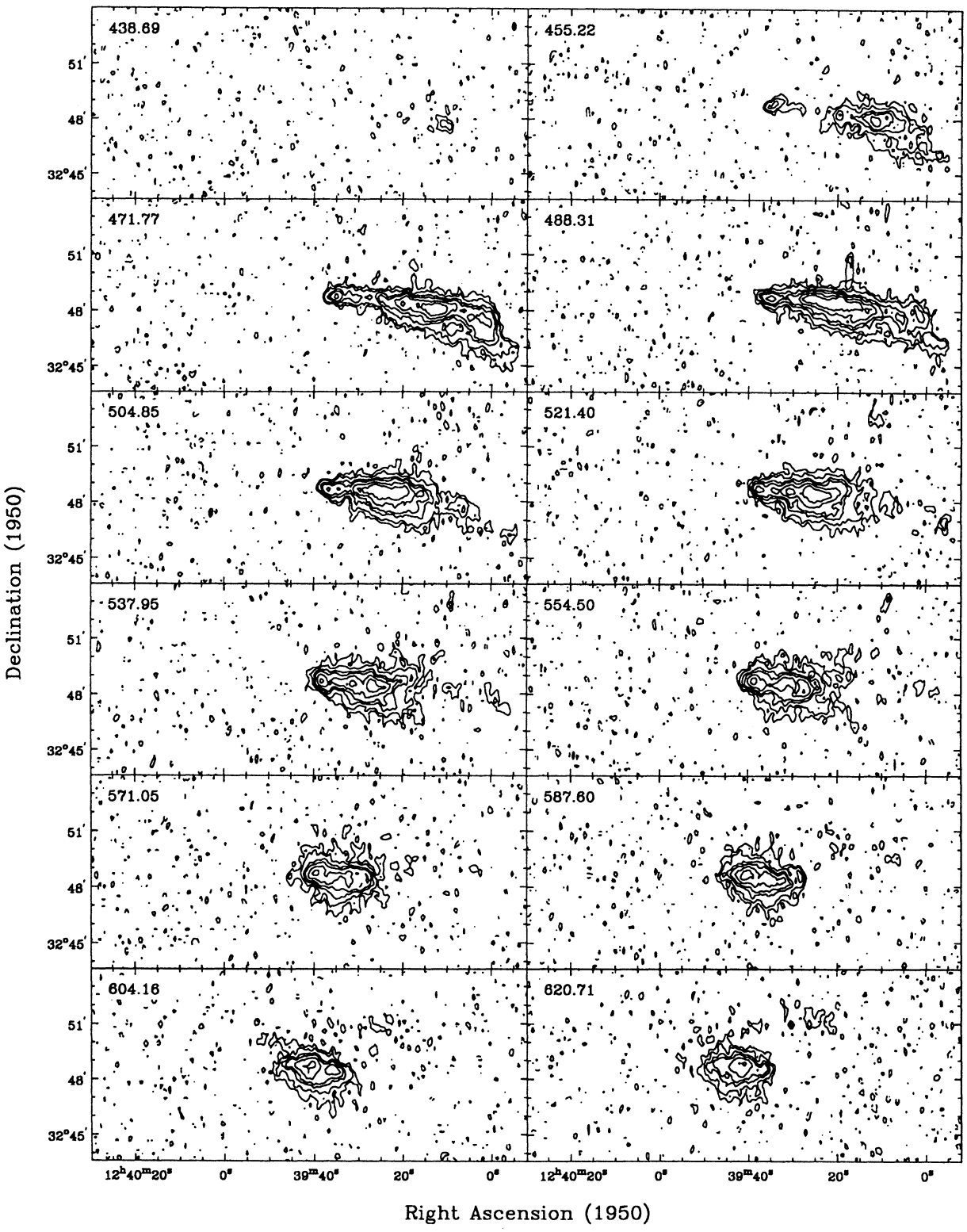

Fig. 3. Channel maps of the NGC 4631 system at $12'' \times 22''$ resolution. Pairs of channels have been summed together, and the mean velocity of the two channels is indicated in each panel. The contour levels are -4, -2, 2, 4, 8, 16, 32, and 48 times the noise in a summed pair of channel maps of 3.8 K. No primary beam correction has been applied

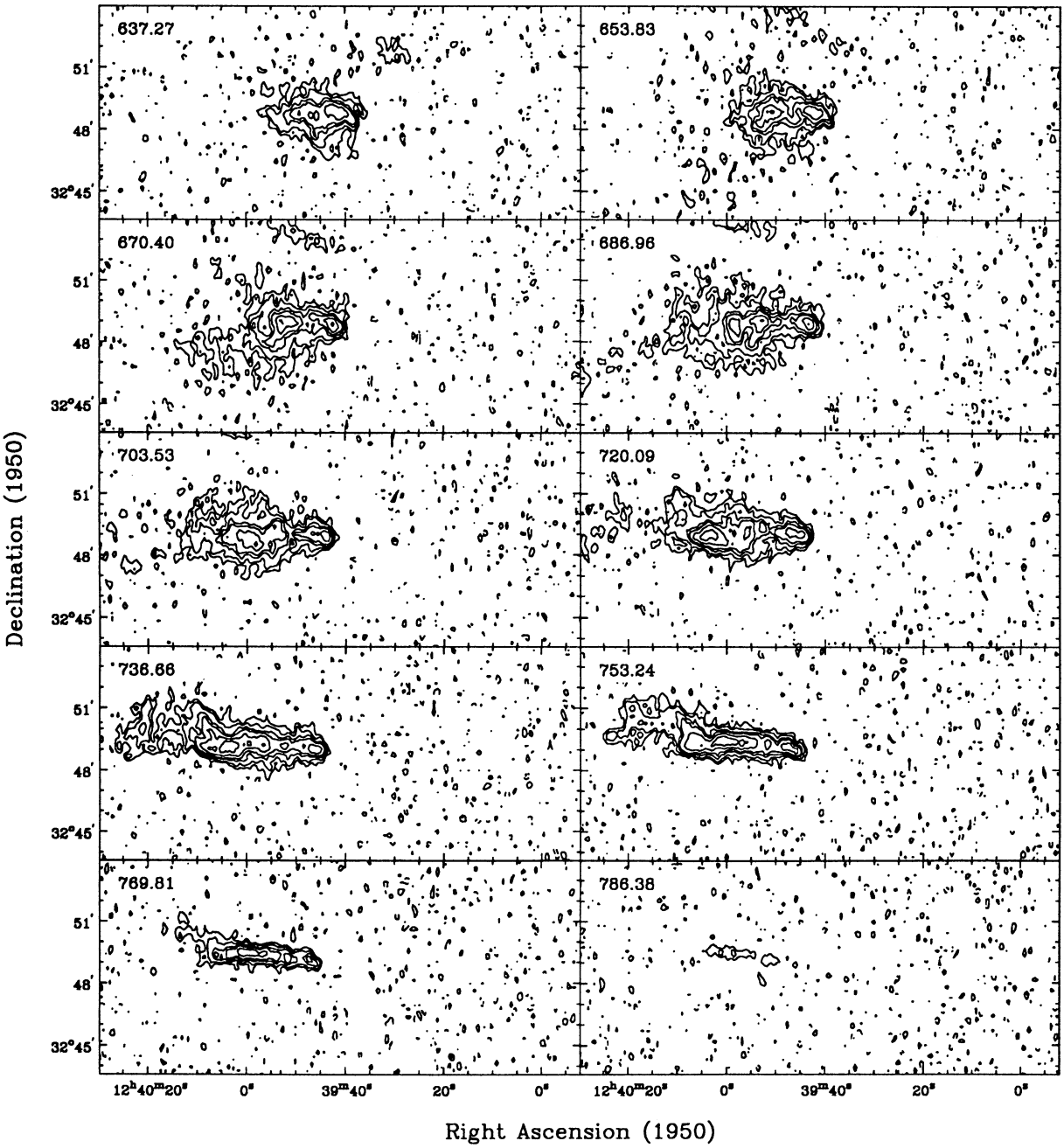

Fig. 3. (continued)

at $V_{\rm hel}$ = 583 km s^{-1}. The connection region can be traced eastwards to R.A. = $12^{\rm h}40^{\rm m}10^{\rm s}$ at $V_{\rm hel}$ = 666 km s^{-1} in the $45'' \times 87''$ and $35''$ channel maps. In the $b-v$ diagrams in Fig. 13, the spur appears as emission well below the plane in most panels from $-6'$ (R.A. = $12^{\rm h}40^{\rm m}1.4^{\rm s}$) to $2'$ (R.A.$12^{\rm h}39^{\rm m}34.5^{\rm s}$). In each panel, the spur joins the disk at velocities appropriate for the outer galaxy (decreasing from 680 to 590 km s^{-1} as it is followed from east to west), and gives the appearance of a southern extension to the outer disk. Other tidal features (see below) cause this extension to persist further to the west. A prominent bifurcation in Spur 2 occurs at the location R.A. = $12^{\rm h}40^{\rm m}0^{\rm s}$, Dec. 32°38′0″, with one component continuing further south, and another looping to the east, where it appears nearly to meet with a feature in Spur 1 at $V_{\rm hel}$= 666 km s^{-1}. Hence, there is a tentative suggestion that Spurs 1 and 2 meet at this location to form a large loop. The physical nature and reality of such a loop is unclear, but it is interesting that such a loop was a feature of the model of the tidal interactions of this group of galaxies by Combes (1978). Emission from the bifurcation region of Spur 2 can be traced over a very large velocity range, 617–716 km s^{-1}, in the $45'' \times 87''$ channel maps. Spur 2 has a projected size of about 60 kpc.

The structure of Spur 3 is best examined in the $45'' \times 87''$ and $35''$ channel maps (Figs. 1 and 2), where it shows up at

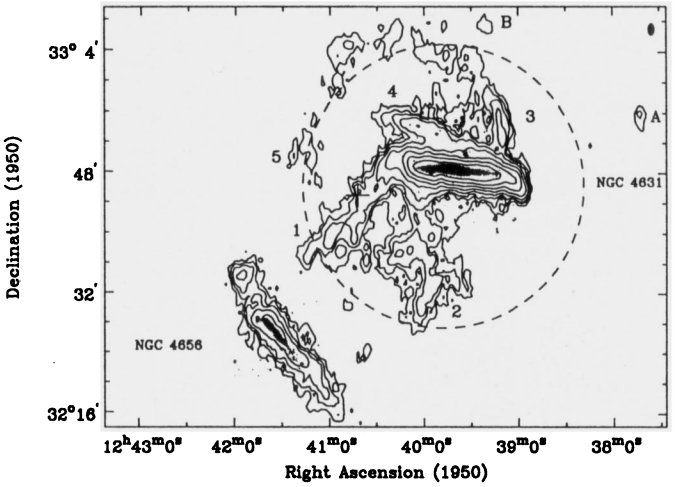

Fig. 4. Contour plot of H I column density at 45″ × 87″ resolution overlaid on optical images of NGC 4631 and NGC 4656. In column density units at the beam center, the contour levels are 0.1, 0.5, 1, 2, 4, 8, 16, 32, and 64 × 10^{20} cm^{-2}. The dashed circle represents the primary beam at half power. H I spurs are labelled "1" to "5". The symbols "+", "A", and "B" show the positions of the three dwarfs. The beam is shown in the top right corner. No primary beam correction has been applied

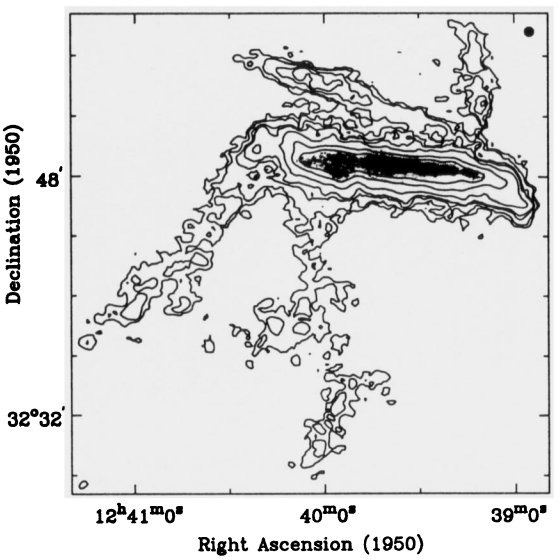

Fig. 5. Contour plot of H I column density at 35″ resolution overlaid on the Hα image of RKH. In column density units at the beam center, the contour levels are 0.5, 1.1, 2.6, 3.7, 7.4, 18.5, 37, and 74 × 10^{20} cm^{-2}. The beam is shown in the top right corner. No primary beam correction has been applied

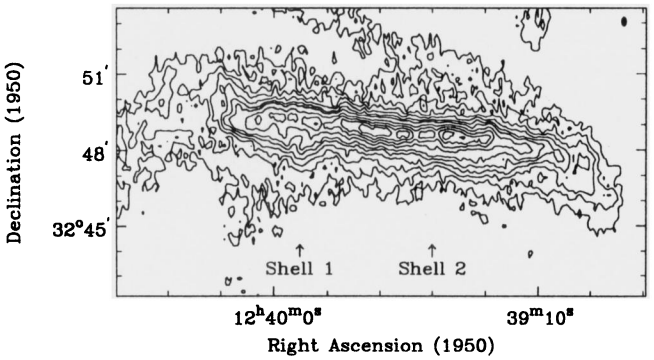

Fig. 6. Contour plot of H I column density at 12″ × 22″ resolution. In column density units at the beam center, the contour levels are 0.9, 5.5, 11.0, 18.4, 27.6, 36.8, 55.2, 73.6, 92.0, and 110.4 × 10^{20} cm^{-2}. The positions of the two supershells are indicated, but note that in this integrated map, only the bottom half of Shell 1 is visible and Shell 2 is not visible at all, due to confusion from other emission along these lines of sight. The beam is shown in the top right corner. No primary beam correction has been applied

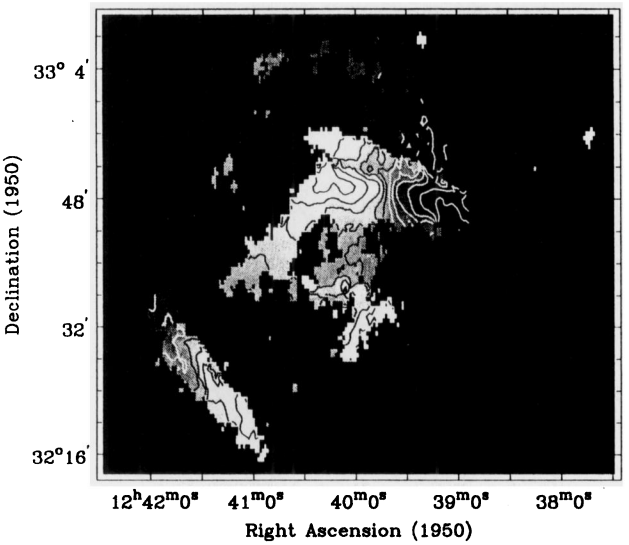

Fig. 7. Grey-scale and contours of the first moment map at 45″ × 87″ resolution. The white contour nearest the center of NGC 4631 is 605 km s^{-1}, and the contours are spaced by 25 km s^{-1}, increasing to the east

velocities between 468 and 567 km s^{-1}, and in the 12″ × 22″ $b - v$ diagrams of Fig. 13, where it appears to join the main disk at an offset of about 5′ west at around $V_{\rm hel}$ = 500 km s^{-1}. Although it joins the galaxy far from the center, this velocity does not correspond to a location at the edge of the disk along this line of sight. Hence, if the spur does in fact join the disk, it may not do so quite at the disk's edge. However, this part of the spur could also have an anomalous velocity and lie elsewhere along the line of sight.

At its lowest velocity (467 km s^{-1}), the channel maps show that the spur does not rise far above the plane. At higher velocities, emission reaches heights of about 30 kpc from the plane, before falling back down and disappearing at 567 km s^{-1}. The emission moves slightly westward with increasing velocity, and by the 567 km s^{-1} channel it has moved 1–2′ to the west. For this position, emission at such a high velocity is not allowed by the normal rotation (compare with Fig. 9 at an offset along the major axis of 6′), so it is doubtful that the high-$V_{\rm hel}$, low-z emission joins the main disk.

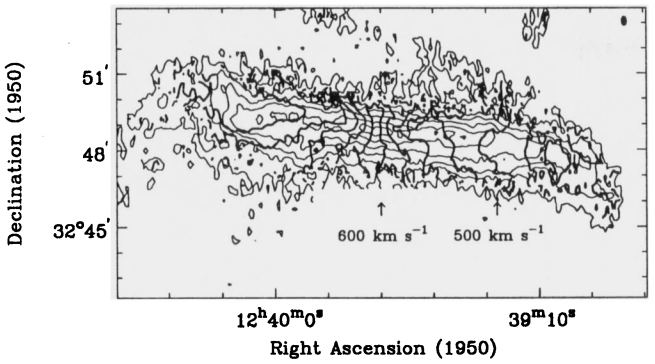

Fig. 8. The thick contours show the first moment map at 12″ × 22″ resolution. The contours are spaced by 25 km s^{-1}, increasing to the east. The thin contours are of H I column density at this resolution. In column density units at the beam center, the contour levels are 1.8, 9.2, 18.4, 36.8, 73.6, and 110.4 × 10^{20} cm^{-2}. The positions of the two supershells are indicated. The beam is shown in the top right corner. No primary beam correction has been applied

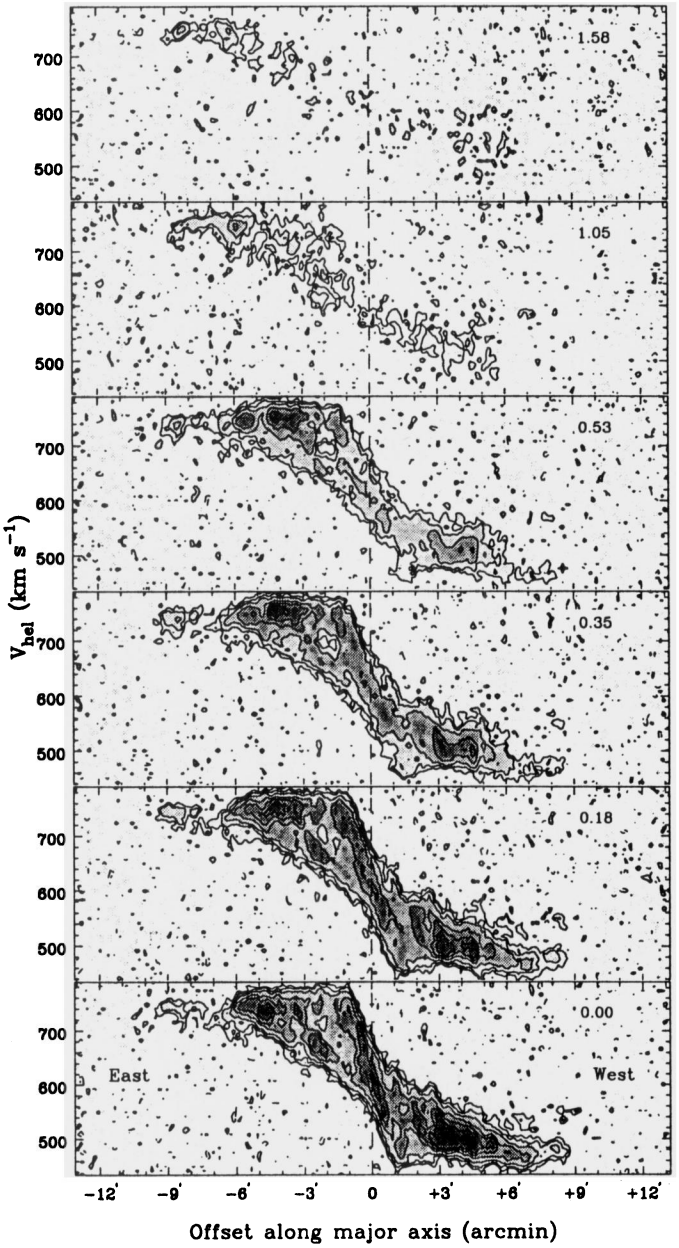

Fig. 9. Position-velocity diagrams parallel to the major axis (P.A. 86°) of NGC 4631 ($l - v$ diagrams), for the midplane and positions above and below, formed from the full-resolution cube. The offset along the minor axis is indicated in each panel. Positive offsets are to the north. The contour levels are −1.5, 1.5, 3, 6, 12, 18, 24, and 36 times the noise of 2.7 K

Spur 4 joins onto the western end of the disk, as can be best seen by tracing it from high to low velocities in the 35″ and 12″ × 22″ channel maps. By V_{hel} = 501 km s^{-1} has moved to a position west and slightly south of the main disk, and is resolved from the disk in this and a few adjacent channels. It eventually joins the main disk from the southwest at about V_{hel}= 468 km s^{-1}. This geometry is the reason that the disk of NGC 4631 appears to be warped sharply downward in the integrated H I maps, in the same way that the interface region of Spur 1 causes the disk to appear to be warped upward. This is not to say that there is no such warp in NGC 4631, it may just be that these two interfaces are part of the warped region. With increasing V_{hel}, Spur 4 can be followed in an east-northeasterly direction up to V_{hel} = 733 km s^{-1}. Its extent is about 60 kpc.

In the blue image of Hummel & Dettmar (1990), diffuse emission can be seen on the northwest side of the galaxy over an extended region to the west of NGC 4627. This emission is roughly coincident with Spur 4, and may be from stars that were stripped from the disk along with this gas.

The newly discovered emission which forms Spur 5 is most clearly seen in the 45″ × 87″ channel maps, although some emission is also present at 35″ resolution. It appears to emanate from the top of Spur 3 at V_{hel} = 517 km s^{-1} moving eastwards and then southwards with increasing V_{hel} until it ends near Spur 1 at V_{hel} = 666 km s^{-1}. Whether Spur 5 is physically related to Spurs 3 and 1 is unclear, but the channel maps give the impression that it forms an extension of Spur 3.

Another small spur can be seen in Fig. 4 at R.A. = 12^{h}39^{m}50^s extending upward from Spur 4. This feature can be best followed at its high-V_{hel} end in the 35″ channel maps, where it emerges from the north-eastern end of the main disk emission at V_{hel} = 683 km s^{-1}. It rises several arcminutes above the plane at lower velocities in the 45″ × 87″ and 35″ channel maps, and falls back down to the disk in the 45″ × 87″ channel maps at V_{hel} = 517 km s^{-1} and R.A. = 12^{h}39^{m}35^s. The high-velocity end of this feature can be seen in Fig. 6 as the diffuse emission above Shell 1, and in many of the $b - v$ diagrams of Fig. 13 on the north side at offsets along the major axis between −2′ and −6′. Since the shell has about the same systemic velocity as this emission, this spur may be related to the event that formed the shell. Yet another small spur emerges from the main disk at V_{hel} = 534 km s^{-1} at a position just south of where Spur 4 joins the disk. It can be followed until V_{hel} = 583 km s^{-1} moving to the southwest. This is best seen in the 35″ channel maps.

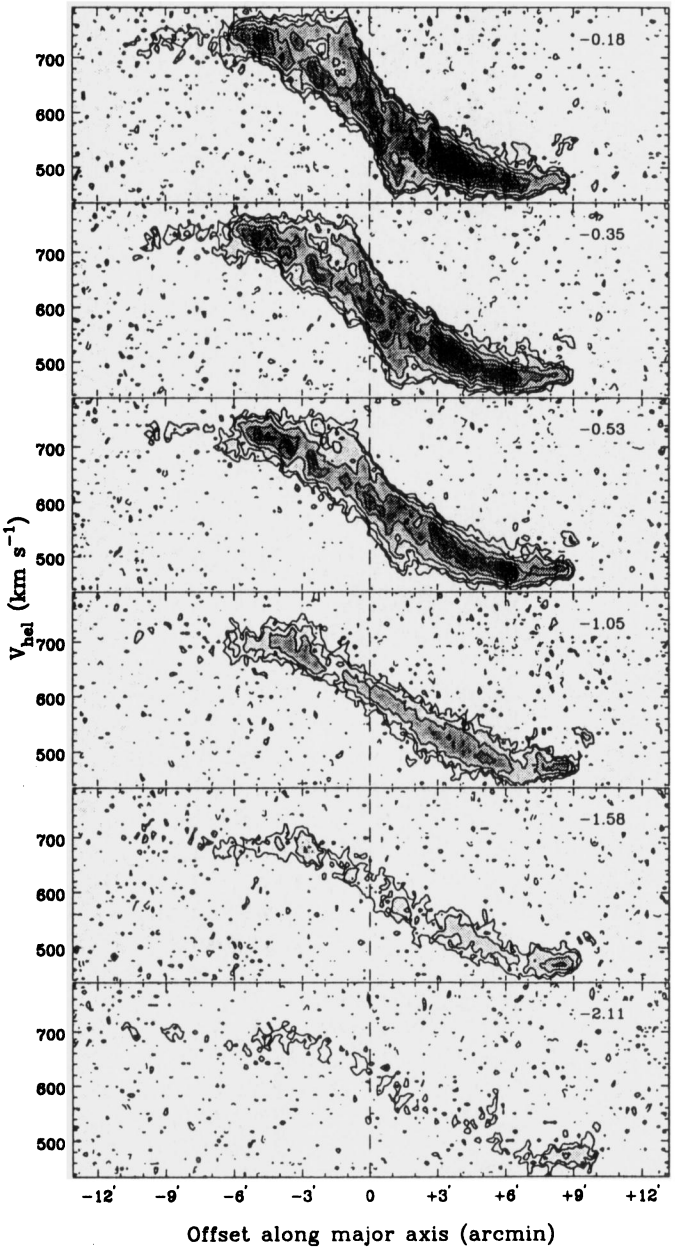

Fig. 9. (continued)

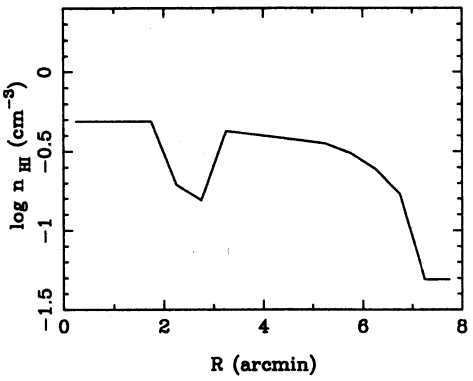

Fig. 10. Density profile for the best model of the H I distribution and kinematics of NGC 4631

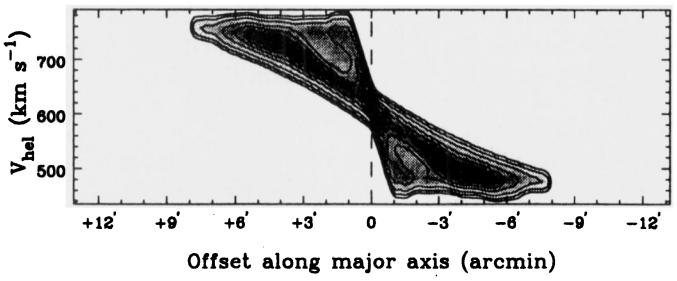

Fig. 11. Midplane $l - v$ diagram for the best model, convolved to $11.5'' \times 21.5''$ resolution. This is to be compared with the midplane diagram of Fig. 7. The contours are the same as in Fig. 7

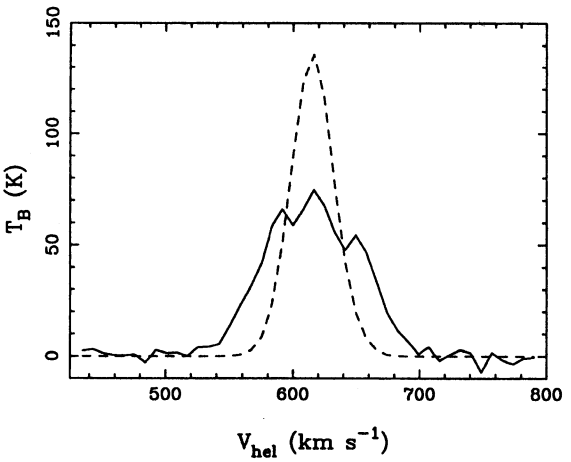

Fig. 12. Velocity profiles at the kinematic center of NGC 4631 from the full-resolution cube (solid line), and the best model (dashed line). Although the observed profile is much broader, the fluxes under the profiles disagree by only 12%

What does all this imply for the origin of the spurs? In the encounter model of Combes (1978), Spurs 2 and 3 could only be explained as gas that was stripped from NGC 4627. However, we have shown that Spur 2 smoothly joins onto the outer disk of NGC 4631, while the base of Spur 3 also coincides with disk emission, albeit at a velocity which does not quite correspond to the edge of the disk. Hence, if the gas in Spurs 2 and 3 once belonged to NGC 4627, it must now be falling onto the outer regions of NGC 4631. The alternative is that all of the spurs originated from NGC 4631. There may be more freedom in assigning an origin to Spur 5, however. It could well be unrelated to NGC 4631 itself.

3.4. Location and origin of gas far from the major axis

We have seen that much of the gas at large distances from the major axis is due to the not quite edge-on aspect of NGC 4631, the rather large z-extent of the outer galaxy gas, and regions where the spurs join the main disk. The question we address here is whether star formation has raised any gas out of the plane, resulting in either a few high-z features or a generally

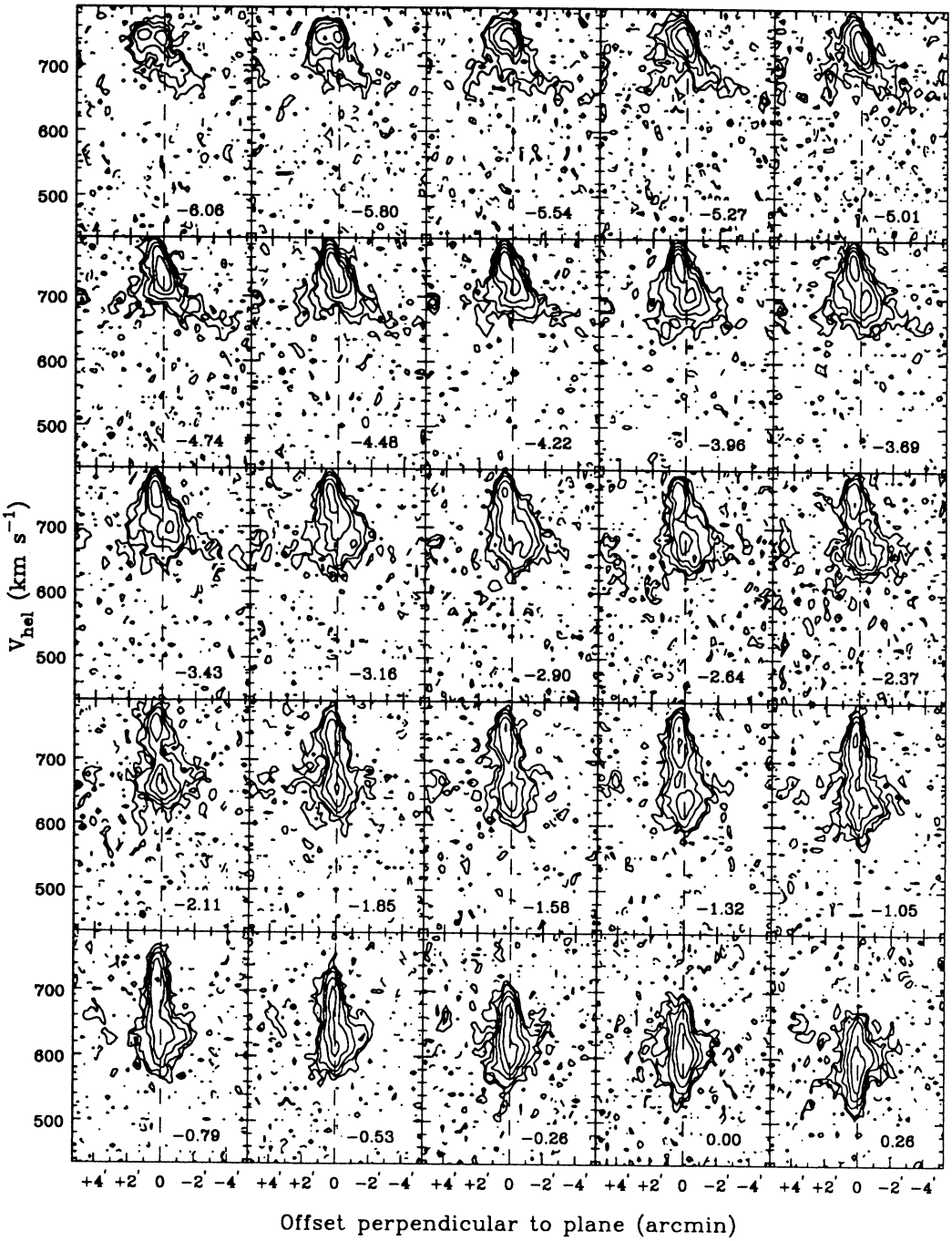

Fig. 13. Position-velocity diagrams perpendicular to the plane ($b - v$ diagrams) of NGC 4631 for distances up to 6′ from the center, made from the full-resolution cube. Three 5.27″ pixels along the major axis have been summed together to produce each diagram. The offset along the major axis in arcminutes is shown in each panel. Negative offsets are to the east. The contour levels −3, −1.5, 1.5, 3, 6, 12, 24, and 48 times the noise in each diagram of 5.5 K

more extended layer. This kind of activity might be expected since NGC 4631 is a galaxy with much ongoing star formation (RKH). In addition, if the radio and X-ray halos are due to disk star formation, then many holes should have been punched through the H I layer. The two H I supershells may represent gas radsed out of the plane by multiple stellar winds and supernovae (see RH), and the nuclear "double-worm" structure seen in Hα may represent a blown out superbubble due to intense nuclear star formation (RKH).

In a simpler edge-on galaxy, one could hope to find clues to the origin of such gas by its velocity structure. Tides, warps, and the effects of an inclination less than 90° should all cause gas to be found far from the major axis at velocities consistent with an outer disk origin. Star formation, which tends to be concentrated at lower radii, should raise out of the plane gas showing

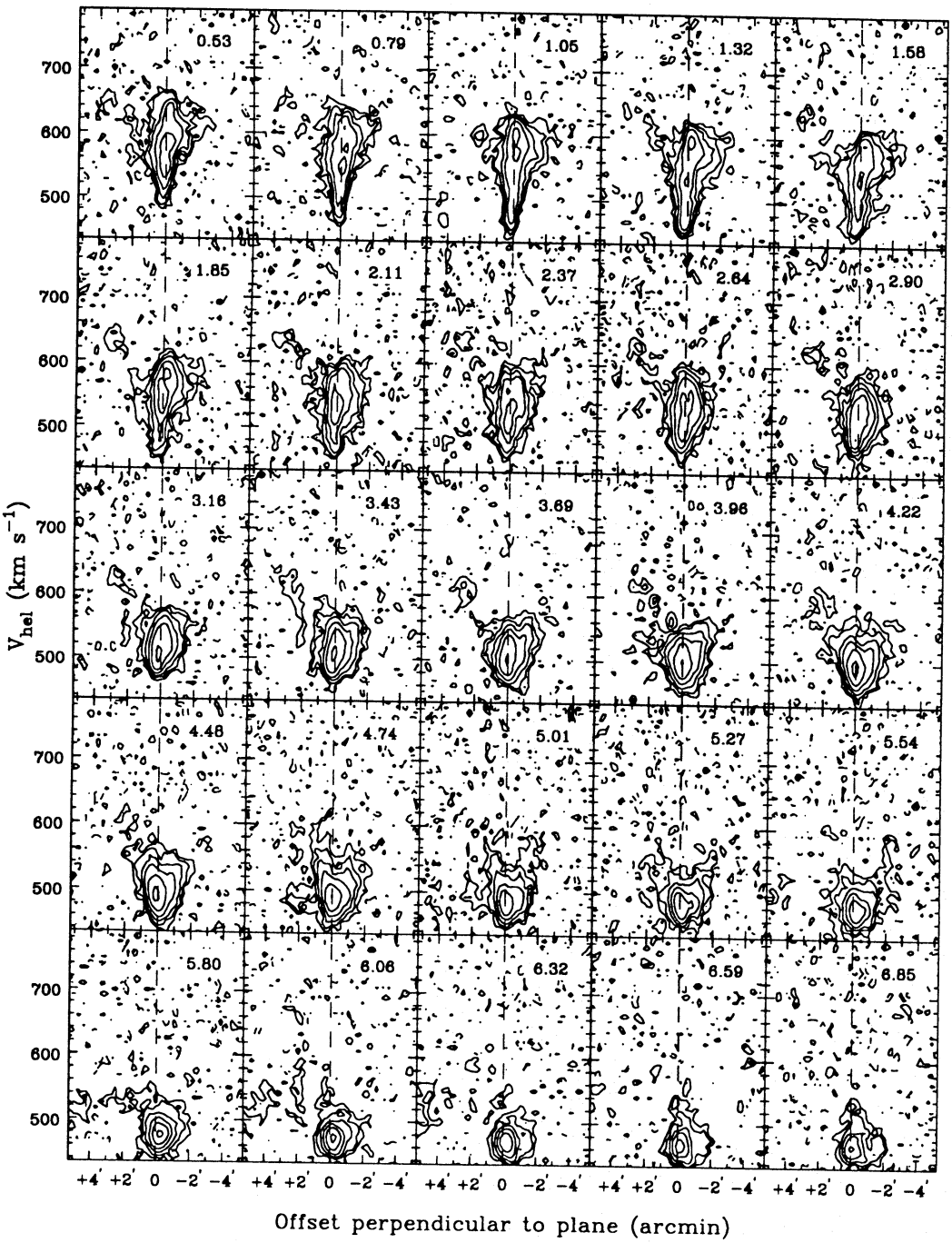

Fig. 13. (continued)

velocities more consistent with an inner disk origin. However, how is massive star formation distributed in NGC 4631?

The Hα distribution (RKH) shows features similar to the H I distribution: the brightest concentrations are in the region of Shell 1 (inferred by RH to be at R = 13 kpc) and at 3–5′ west of the nucleus. There is also an enhancement of bright star-forming complexes in the central 3′. Bright Hα emission is found up to 6′ or 13 kpc from the center. This morphology suggests that the outer galaxy has much associated star formation, but the inner disk is also forming stars. In fact, a spectrum of a bright H II region at the eastern end of the inner disk (Roy et al. 1991), just west of where the gas layer is pinched, shows a velocity expected for an inner disk origin. It is likely that extinction is greater toward the inner disk and it is forming more stars than is suggested by the Hα intensity. A Fabry-Perot study or more complete optical spectroscopy would better reveal the distribution of star formation.

As far as the outer galaxy is concerned, its large scale-height of 500–1000 pc may be accompanied by a large velocity dispersion due to star formation and/or tidal disturbances. Very

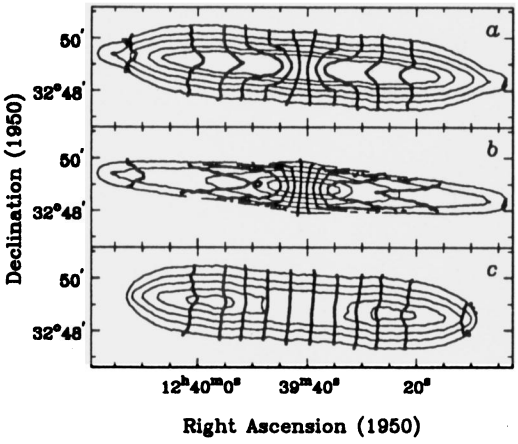

Fig. 14. In **a** is shown the total H I column density and velocity contours of the model which best reproduces the midplane $l - v$ diagram of NGC 4631. The contours are the same as in Fig. 6. In **b** and **c** are shown the best-fit inner and outer components, respectively. Note that the "inner disk" actually has the larger radial extent, due to its slow falloff in density with radius. The assignment of emission at such large radii to one or the other model components is essentially arbitrary

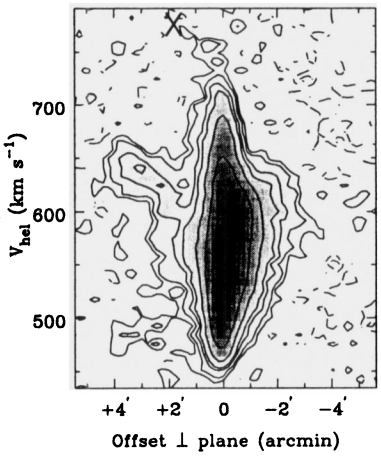

Fig. 15. A $b - v$ diagram from the 35″ resolution cube to the region around NGC 4627. The data were summed along the major axis over the R.A. range $12^h39^m27^s$ to $12^h39^m44^s$. An X has been plotted at the position and velocity of NGC 4627. The contour levels are −3, −1.5, 1.5, 3, 6, 9, 18, 36, 54, and 72 times the noise in the diagram of 6.4 K. Positive offsets are to the north. The bright emission well to the north of the midplane is from Spur 4, and clearly has a different velocity from NGC 4627

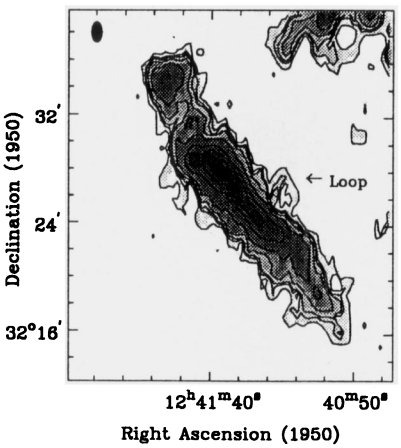

Fig. 16. Total H I column density in NGC 4656 at 45″ × 87″ resolution. In column density units corrected for primary beam attenuation at the center of NGC 4656, the column density contour levels are 0.8, 2.3, 3.1, 4.6, 7.6, 15.3, 22.9, 30.6, and 38.2×10^{20} cm^{-2}. The apparent loop is indicated

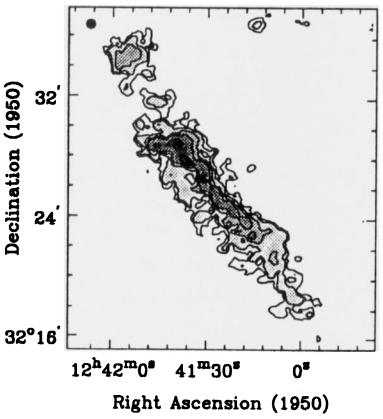

Fig. 17. Total H I column density of NGC 4656 at 35″ resolution. In column density units corrected for primary beam attenuation at the center of NGC 4656, the contour levels are 2.4, 5.9, 11.8, 18.9, 35.5, and 70.9×10^{20} cm^{-2}

roughly, since the scale-height should scaje as $\sigma_v/\sqrt{\varrho_0}$ (where σ_v is the vertical velocity dispersion and ϱ_0 is the total mass density in the midplane; Spitzer 1978), and since ϱ_0 should scale roughly as the square of Θ_0^2, the rotation speed (at least for galaxies with similar mass distributions, because the mass should scale roughly as Θ_0^2, e.g. Fich & Tremaine 1991), we expect the scale-height to scale as σ_v/Θ_0^2. In the Milky Way, at about $R = 11$ kpc, the rotation speed is 220 km s^{-1}, and the FWHM of the atomic layer is about 500 pc (Burton 1992), which translates to a scale-height of 350 pc. If σ_v in the outer galaxy equalled the solar neighborhood value of 8 km s^{-1} (Kulkarni & Heiles 1987), we would expect a scale-height of 550 pc in NGC 4631. Hence, the modelled scale-height of 500–1000 pc indicates that the vertical dispersion may be equal to or somewhat higher than the solar neighborhood value, suggesting that star formation has not stirred up the gas much more than in the solar neighborhood. This constraint is not too significant, however.

In the outer parts, then, star formation may or may not carry gas high above the plane, but regardless, there are many other confusing sources of emission far from the major axis. To show these clearly, and to search for high-z H I which we can associate with the *inner disk* through its kinematics, we return to the high-resolution $b - v$ diagrams of Fig. 13.

The diagrams at intermediate distances from the major axis center show a characteristic shape, with the inner disk component (which shows up at velocities around 750 km s^{-1} on

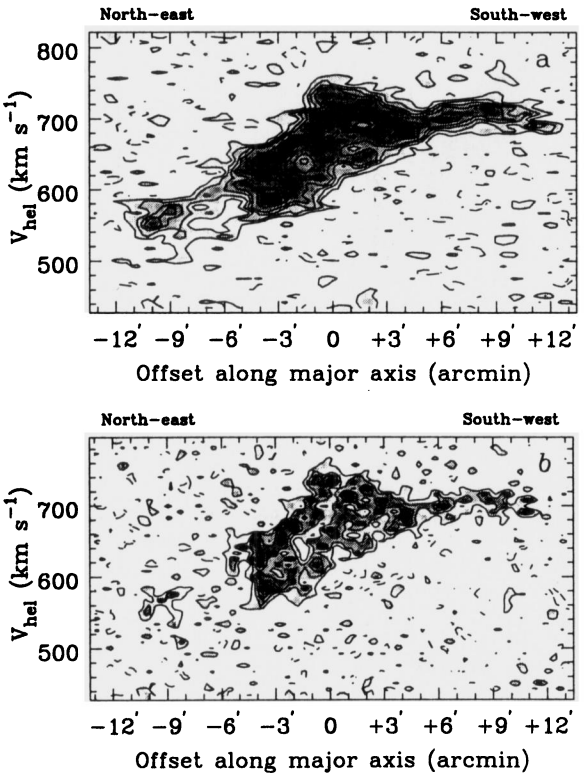

Fig. 18a and b. Major axis $l-v$ diagram for NGC 4656 at **a** 45″ × 87″ and **b** 35″ resolution. The northeast end is on the left side of each figure. The contours in **a** are −1.5, 1.5, 3, 4.5, 6, 9, 12, and 15 times the noise of 0.26 K, and in **b** −1.5, 1.5, 3, 4.5, 6, 7.5, and 9 times the noise of 0.66 K. Note the velocity extent of the emission in the central regions

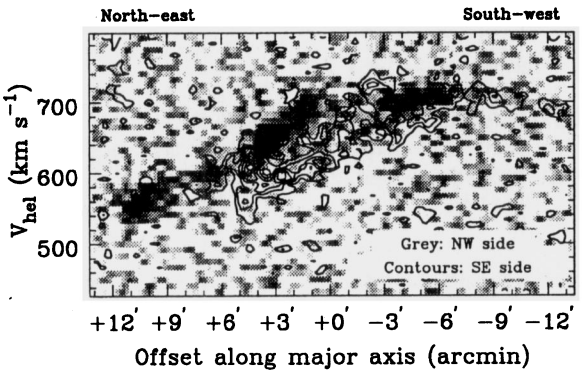

Fig. 19. $l-v$ diagrams above and below the major axis. Emission from 30″–90″ above the plane on the south-east and north-west sides has been averaged to produce the grey scale and contours, respectively. The northeast end is on the left side of each figure. In the central regions, high and low velocity emission clearly belong to opposite sides of the midplane

the east side and 500 km s^{-1} on the west side) having a much smaller extent in the minor axis direction than the outer galaxy (which shows up at velocities closer to the systemic velocity). Our modelling showed this to be due to inclination and the larger z-extent of the outer galaxy. Near the center of the major axis, both components are seen at the same velocities, while towards

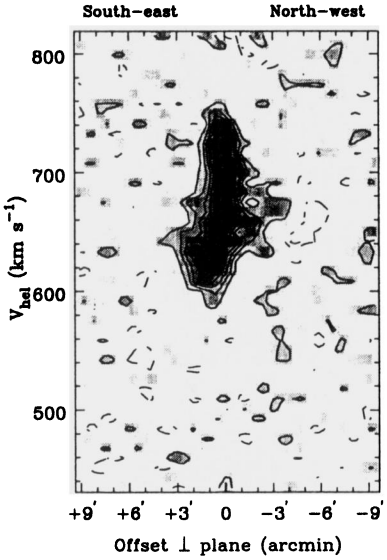

Fig. 20. A $b-v$ diagram integrated over the extent of the apparent loop above the center of the major axis on the north-west side of NGC 4656. The integration is over 7 pixels or 226″. Positive offsets refer to the south-east side of the galaxy. The loop is found between offsets −1′ and −4′. The contours are −3, −1.5, 1.5, 3, 4.5, 6, and 12 times the noise in the diagram of 1.1 K. The only emission from the loop that can be considered real has the morphology of a spur and occurs at velocities consistent with the spread in the disk material below

the ends of the major axis, the outer galaxy dominates, and the extent perpendicular to the major axis is large there.

Some of the spurs constitute additional sources of emission far above and below the major axis. We have already seen that Spur 2 joins the disk over an extended region along the south side. In most $b-v$ diagrams at offsets less than 2.37′ along the major axis, this gas appears as an extra extension to the south at velocities corresponding to outer disk gas. Further westward along the major axis (toward greater offsets), extended emission can also be seen from the small spur south of Spur 4 (see above). Along the north side, most of the emission far from the midplane is due to the outer galaxy, Spurs 3 and 4, and the small spur above Shell 1.

At some locations, however, high-z features can be seen with velocities of inner disk material. For instance, at an offset of −1.85′ in Fig. 13, a feature can be seen at V_{hel} = 680–740 km s^{-1} which certainly appears to emerge from the inner disk rather than the outer component. The velocity decreases with height above the plane by some 30 km s^{-1}. In Fig. 6, this feature extends out of the pinched region of the H I layer (at R.A. = 12^{h}39^{m}50^s). There is no coincident Hα emission, but there is a faint worm 15″ to the east which may be related. Hence, we suggest that this feature could well be gas raised out of the plane by star formation. Other features can be seen in some panels on the north side at offsets between 1.58′ and 2.90′ and around V_{hel} = 500 km s^{-1}, between −1.58′ and −1.05′ around V_{hel} = 700 km s^{-1}, and between −0.53′ and 0.00′ around V_{hel} = 680 km s^{-1}. The second of these is directly above Shell 2, and may be related to that structure. The

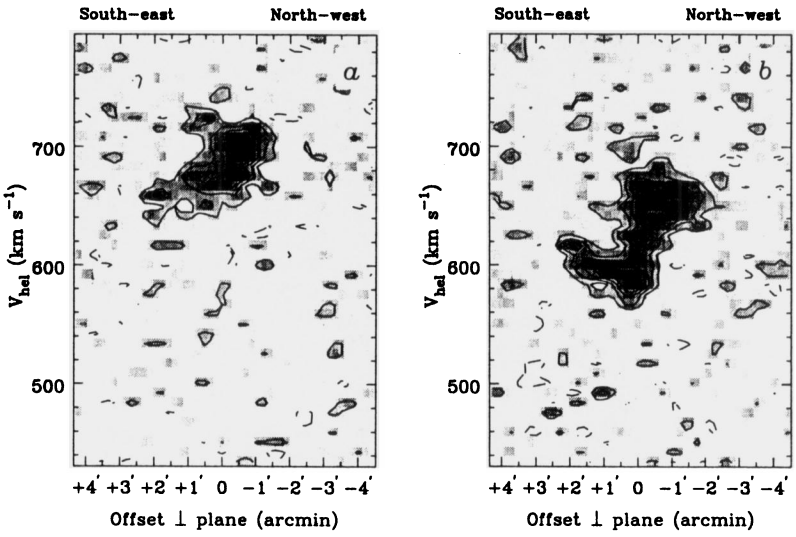

Fig. 21a and b. $b - v$ diagrams for two worms extending out of the plane of NGC 4656. The central position of **a** is R.A.$12^h41^m19^s$ Dec. 32°23′21″, and of **b**, R.A.$12^h41^m37^s$ Dec. 32°27′55″. Both diagrams represent emission integrated along the major axis over 7 pixels or 74″. Positive offsets refer to the south-east side of the galaxy. The contour levels in each case are −3, −1.5, 1.5, 3, 4.5, 6, and 12 times the noise in the diagrams of 3.1 K

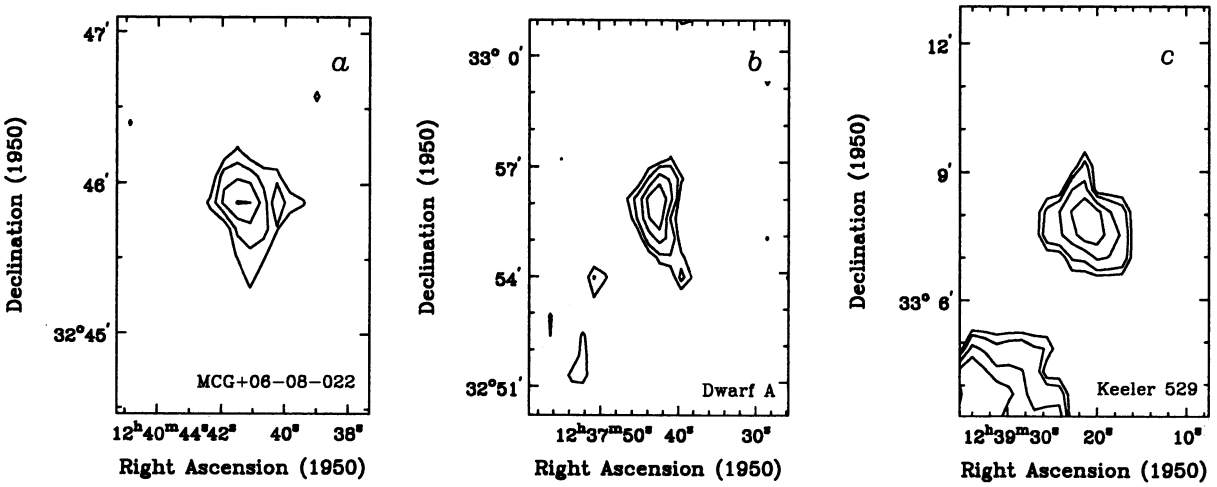

Fig. 22. Contour plots of H I column density from **a** MCG+06-08-022 at 12″ × 22″ resolution (contour levels corrected for primary beam attenuation are 1, 2, 3 and 4 times 2.35×10^{20} cm^{-2}), **b** Dwarf A at 45″ × 87″ resolution (contour levels are 1, 2, 4 and 6 times 2.4×10^{19} cm^{-2}), and **c** Keeler 529 at 45″ × 87″ resolution (contour levels are 1, 2, 4 and 6 times 6×10^{18} cm^{-2})

column densities of these features are a few times 10^{20} cm^{-2} in each panel.

We think it likely that the Hα double-worm of RKH is located near the nucleus of the galaxy, and is not an outer disk feature seen in projection close to the center. If so, then the above-mentioned inner disk feature between −0.53′ and 0.00′ demonstrates that there is high-z gas in the central regions coincident with this structure. Larger amounts of gas far from the major axis in the central few panels of Fig. 12 can be found at velocities near systemic, implying that they could arise from anywhere along the line of sight, It is therefore difficult to make an association between any of these features and the Hα structure.

In summary, then, we have found a few high-z features whose kinematics suggest an origin in the inner disk and which are likely to be due to star formation. These do not comprise the bulk of the H I far from the major axis, however, and are not responsible for the generally ragged appearance of the H I layer at high-resolution. This emission is almost entirely due to the outer disk. The relatively weak galactic potential should result in a large scale-height, but tidal features such as Spur 2 are additional sources of high-z gas and disturbances, and outer-galaxy star formation may also play a role.

3.5. The dwarf elliptical companion NGC 4627

It has been suggested that NGC 4627 was once a gas-rich galaxy that had its gas stripped by the encounter with NGC 4631 (Combes 1978). A nuclear spectrum (quoted by Caldwell 1983) reveals strong Balmer absorption lines, which suggest young stars. CCD images by Vigroux et al. (1985) show that the nucleus is resolved into four concentrations which are bluer than the surrounding emission, again suggesting young stars. Other evidence that the galaxy has been disturbed by the encounter comes from the twisted isophotes, which can be seen in Fig. 10 of Hummel & Dettmar (1990). RKH did not find any Hα emission from NGC 4627, but the continuum had been slightly oversubtracted,

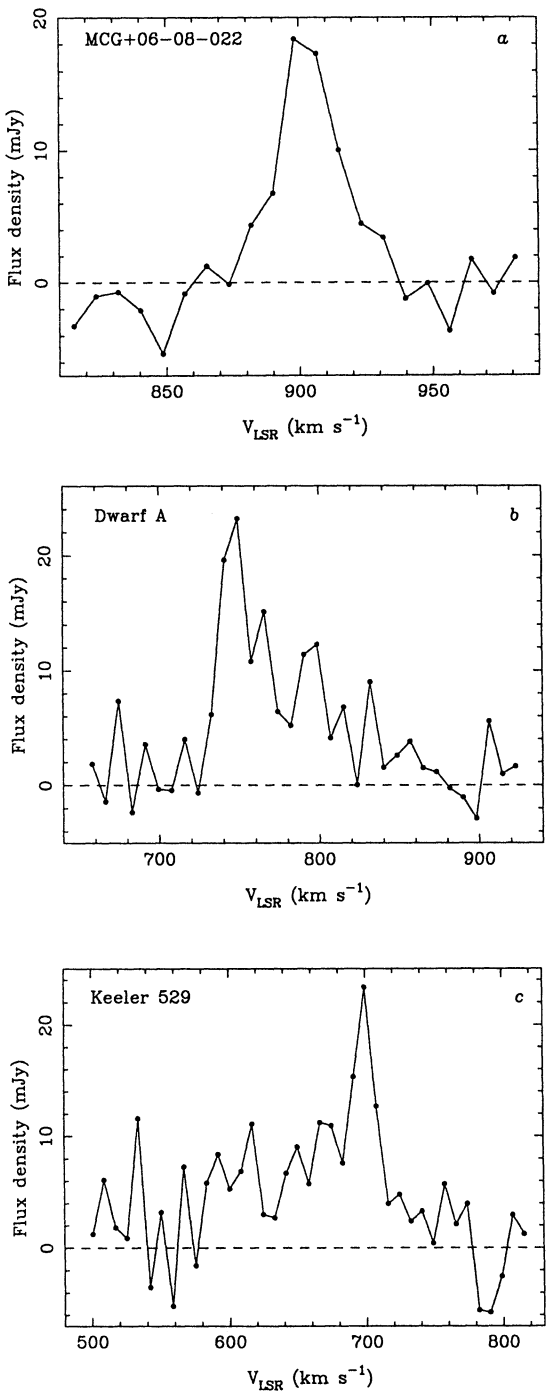

Fig. 23. Integrated spectra of **a** MCG+06-08-022 at $12'' \times 22''$ resolution, **b** Dwarf A at $45'' \times 87''$ resolution, and **c** Keeler 529 at $45'' \times 87''$ resolution

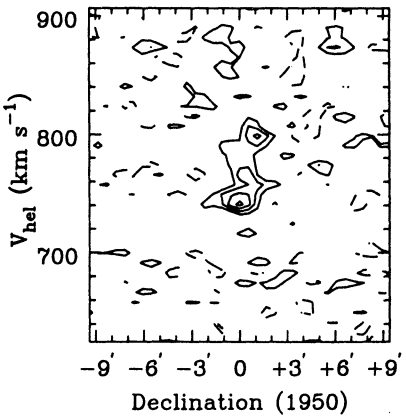

Fig. 24. Declination-velocity diagram of Dwarf A, integrated over five pixels in Right Ascension. The contour levels are -1.5, 1.5, 3, 6 and 9 times the noise of 1.0 K

suggesting that the Hα-to-continuum ratio in NGC 4627 is different from that of the foreground Galactic stars used to carry out the subtraction. Hence, one cannot rule out diffuse Hα emission distributed like the stars. No patchiness was seen in Hα corresponding to the blue nuclear features, but the latter were seen under good seeing conditions ($0.6''$), whereas the pixel size of the Hα image is much larger ($1.2''$). Hence, Hα emission from NGC 4627 cannot be firmly ruled out. In Combes' (1978) simulation of the encounter, Spurs 2 and 3 could only be explained as being gas that once belonged to NGC 4627. As an aside, however, it should be noted that an accurate velocity of NGC 4627 was not available at that time, and the velocity used by Combes 660 km s^{-1}, is much lower than the value of 765 ± 29 km s^{-1} reported in the *Third Reference Catalog of Bright Galaxies* (de Vaucouleurs et al. 1991). Hence the details of the encounter model may have to be revised.

Although there is gas at the position of NGC 4627 (R.A. $12^h\ 39^m\ 33^s$, Dec. 32° 50′ 48″), no emission can be unambiguously associated with the galaxy. Spur 4 crosses a position $\sim 1'$ north of NGC 4627 at about $V_{hel} = 633$ km s^{-1} (see Fig. 5), and is unlikely to be related to the dwarf elliptical. In the $35''$ total intensity map, high-z emission from NGC 4631 is coincident with the position of the NGC 4627 (marked with an "X"), but a $b-v$ diagram for this region of NGC 4631 (Fig. 15) shows that this emission is in the velocity range 550–640 km s^{-1} – much lower than that of the dwarf companion. In the full-resolution data cube, these features have been resolved out so that no emission is coincident with NGC 4627. We have searched the data cubes without success for emission from the vicinity of the dwarf at higher velocities than shown in the figures. We conclude that NGC 4627 has no detectable associated emission at or near its velocity, and that, if it did once contain gas, the gas must now be completely detached from the system (now constituting some of the spurs, for example) since no detectable tail of gas can be seen extending from it.

3.6. The edge-on companion NGC 4656

Total intensity maps of NGC 4656 at $45'' \times 87''$ and $35''$ are presented in Figs. 16 and 17. The H I layer of this galaxy has also been disturbed by the encounter. There is a bright, distinct feature at the north-east end of the disk, a sharp bend at the north-east end of the main emission, and several worms extending up to 5 kpc out of the disk. The worms are mostly on the south-east side, but the most prominent high-z feature is an apparently complete loop on the north-west side, above the center of the galaxy. The worms are better seen in the higher resolution map,

but there the loop is almost completely resolved away. Optically, the blue Palomar Optical Sky Survey (POSS) plate shows that the north-eastern half of the disk is much brighter than the south-western half, and the sharp bend at the north-east end is clearly seen. A faint arm runs parallel to the south-western half of the disk, but displaced to the south-east by about $1'$.

Before examining these small-scale features, we concentrate on the structure of the main disk. Figure 18 shows a major axis $l-v$ diagram from cubes at the two aforementioned resolutions. The figure suggests a systemic velocity of $V_{\rm hel} \approx 650\,{\rm km\,s^{-1}}$. Although the basic signs of normal rotation are present, the kinematics are obviously much more complex. Evidence for differential rotation is only present on the south-west side over a limited distance. The feature at the north-east end seems to participate in the general rotation. More interesting is the large velocity width over most of the major axis, especially the inner parts. In this respect, NGC 4656 is similar to NGC 4631, except that here the effect is more dramatic. For a disk with no non-circular motions, the velocity width should be very small near the kinematic center, yet in the central parts of NGC 4656, the velocity spread of the emission is $> 100\,{\rm km\,s^{-1}}$ and there are hints of a double-peaked velocity structure with peaks separated by some $80\,{\rm km\,s^{-1}}$. Clearly, non-circular motions are present. Given the high inclination, one can assume that these motions are in the plane.

Further evidence as to the nature of the motions is provided by $l-v$ diagrams displaced above and below the midplane (Fig. 19). In this figure, the grey-scale represents emission from $30''-90''$ above the plane on the south-east side, while contours represent emission from the same heights on the north-west side. The emission clearly splits up into two distinct kinematic components on either side of the midplane. The most natural explanation for this splitting is that the galaxy is not quite edge-on, and we are seeing the different (peculiar) kinematic signatures of the near and far sides.

Tidal disturbances are a possible explanation for this kinematic structure. NGC 4656 may consist primarily of two tidal spiral arms with large opening angles leading to strong deviations from circular motion. The south-eastern arm would contain gas streaming towards us, while the north-western arm would consist of receding gas. The faint optical arm mentioned above could be the counterpart of the south-eastern H I arm.

Alternatively, NGC 4656 could be a ring galaxy of the Cartwheel type seen not quite edge-on. Ring galaxies owe their structure to a collision with a companion near the center, which causes a density wave to propagate radially outwards, sweeping up gas into starbursting rings as it does so. In such galaxies, radial oscillations are excited in the gas, and density peaks occur where inflowing and outflowing gas are brought together (Appleton & Struck-Marcell 1987). The line-splitting suggests that all of the atomic component, on both the near and far side of the ring, would have to be in the outflowing part of the radial oscillation cycle, but this seems to be expected from simulations (see Fig. 2 of Appleton & Struck-Marcell 1987; alternatively, all of the atomic gas could be inflowing). There is no obvious sign of a nearby intruder on the POSS plates, but models show that the rings can persist for more than $\sim 10^8$ yr (e.g. Appleton & Struck-Marcell 1987), so the intruder could now be many kpc away, making the dwarfs potential candidates. If the ring is circular in the plane of the galaxy, then its extent perpendicular to the major axis of $\sim 1'$ suggests an inclination of 80–85°.

We return now to the structure that appears as a complete loop on the north-west side above the center of the galaxy in the $45'' \times 87''$ total intensity map. A $b-v$ diagram, integrated along the plane over the extent of the feature, is shown in Fig. 20. The high-z emission extends over many channels, at velocities where disk gas also emits (the weaker features at $V_{\rm hel} \lesssim 600\,{\rm km\,s^{-1}}$ do not contribute to the total intensity map). The mass of the structure is $\sim 3 \times 10^7 M_\odot$. The loop-like appearance is at very low signal-to-noise levels, however, and until higher sensitivity observations of NGC 4656 become available, the loop morphology remains a tentative conclusion.

The worms have a velocity structure which suggests an outer disk origin. Figure 21 shows $b-v$ diagrams from the $50''$ cube (again averaged over 3 pixels along the plane) through two of the worms. Compared to the lower-z velocity component, worms on both sides of the kinematic center have velocities closer to $V_{\rm sys}$. This velocity structure would arise if the worms were outer-disk features. Hence, they are likely to be due to tidal effects. The location of massive star formation in NGC 4656 is unknown, but may also be concentrated in an outer galaxy structure as suggested for NGC 4631. If so, then again, it is difficult to distinguish the possible origins of high-latitude gas from its kinematics alone.

Since NGC 4656 lies at the 15% power point of the WSRT primary beam, sensitivity is not as high as desired. Many of these issues, such as the disk structure of NGC 4656 and the reality of the high-z loop, could be better addressed with 21-cm line observations pointed on this galaxy.

3.7. The three dwarfs with H I

RH noted two small dwarfs with H I in the NGC 4631 system, MCG+06-28-022 (labelled "+" in Fig. 4) and an optically unidentified dwarf (labelled "A"). A third dwarf with H I, not reported in RH, has since been discovered upon closer inspection of the data. It is optically identified as Keeler 529, and is labelled "B" in Fig. 4. Properties of MCG+06-28-022, Dwarf A and Keeler 529 are summarized in Table 3. Total intensity maps of the dwarfs are shown in Fig. 22, and integrated spectra in Fig. 23. MCG+06-28-022 has a very small H I size of about 800 pc, and while coincident with Spur 1 (Fig. 4), it has a velocity different by $200\,{\rm km\,s^{-1}}$. It is not visible in Fig. 5 because the velocity range used in making these maps does not extend up to the velocity of the dwarf.

The spectrum of Dwarf A is very asymmetric and suggests unusually broad emission, and close inspection of the channel maps reveals that the emission from 740–810 km s^{-1} is believable. There is slight velocity structure along the Declination axis, as the integrated position-velocity diagram in Fig. 24 shows. The extent along this axis is ~ 2 kpc. The dwarf is not well detected in higher resolution maps. Optically, the dwarf is

Table 3. HI properties of features in the NGC 4631 system

Large Galaxies	Central Position[a] (1950.0)	HI Line Flux[b] (Jy km s^{-1})	HI Mass[c] ($M_\odot$)	V_{sys} (km s^{-1})	Vel. range (km s^{-1})
NGC 4631	R. A. $12^h\ 39^m\ 41.2^s$ Dec. 32° 48′ 56″	425	$7 \times 10^9\ M_\odot$	615	430–790
NGC 4656	R. A. $12^h\ 41^m\ 31.6^s$ Dec. 32° 26′ 31″	300	$5 \times 10^9\ M_\odot$	660	530–750
Detected dwarfs	**HI Position (1950.0)**	**HI Line Flux[b] (Jy km s^{-1})**	**HI Mass[c] ($M_\odot$)**	**V_{sys} (km s^{-1})**	**ΔV (FWHM) (km s^{-1})**
MCG+06-28-022	R. A. $12^h\ 40^m\ 41.0^s$ Dec. 32° 46′ 2″	1.2	2×10^7	900	30
A	R. A. $12^h\ 37^m\ 41.0^s$ Dec. 32° 55′ 00″	5.5	9×10^7	775	~ 50
Keeler 529	R. A. $12^h\ 39^m\ 21.0^s$ Dec. 33° 7′ 46″	1.2	2×10^7	695	~ 25
Spurs	**Proj. length (kpc)**	**HI Line Flux[b] (Jy km s^{-1})**	**HI Mass[c] ($M_\odot$)**	**Vel. range (km s^{-1})**	
1	60	40	$6 \times 10^8\ M_\odot$	620–770	
2	60	50	$8 \times 10^8\ M_\odot$	590–740	
3	30	25	$4 \times 10^8\ M_\odot$	470–570	
4	60	55	$9 \times 10^8\ M_\odot$	470–730	
5	120	20	$3 \times 10^8\ M_\odot$	520–680	

[a] Reference for adopted position of NGC 4631 is Ekers & Sancisi (1977), and for NGC 4656, Gallouët, Heidmann & Dampierre (1973).
[b] Corrected for primary beam attenuation.
[c] All masses assume small optical depth and include the helium content.

Table 4. Parameters of the best model of the HI distribution in NGC 4631

	Inner Disk		Outer Disk	
V_{sys} (km s^{-1})	617		610	
σ_v (km s^{-1})	15		15	
Scale-height (pc)	500		800	
Incl. (deg.)	85		85	
Major axis P.A. (deg)	86		86	
Rotation speed (km s^{-1})	145 $R/2$	$R < 2$	$110 + 8(R - 7)$	$7 < R < 11$
(radii in kpc)	145	$R > 2$	140	$R > 11$
Density Profile (cm^{-3})	0.5	$R < 4$	0	$R < 7$
(radii in kpc)	0.12	$4 < R < 9$	0.3	$7 < R < 13$
	0.05	$9 < R < 17$	0.15	$13 < R < 15$

barely visible on the POSS plates, and we very roughly estimate an M_B of -11 to -12. From the Tully-Fisher relation, galaxies with an inclination-corrected ΔV (FWHM) of $\sim 50\,\mathrm{km\,s^{-1}}$ should have $M_B \sim -15$ (Broeils 1993). Hence, the large velocity extent may be indicating that some of the gas has been stripped away from the galaxy. Keeler 529 has a size of about 3 kpc. A close inspection of the channel maps reveals that the apparent low-level emission in the spectrum of Keeler 529 at $V_{\mathrm{hel}} = 670\,\mathrm{km\,s^{-1}}$ is not significant, so that the velocity width is comparable to that of MCG+06-28-022.

4. Concluding remarks

The main conclusions from this work are as follows:

(1) The main 21-cm line emission from NGC 4631 is due to an inner disk and an outer density enhancement, which may simply be a spiral pattern. The rotation speed is about $140\,\mathrm{km\,s^{-1}}$. The inner disk is warped upwards on both the east and west sides. The outer galaxy has a greater extent along the minor axis. This is mostly due to the inclination being less than 90°, a greater scale-height than the inner disk, and the connection region of Spur 2 to NGC 4631. The supershells reported by RH appear to be associated with the outer disk.

(2) Spurs 1 and 4 connect onto the eastern and western ends of the major axis, respectively. Spur 1 does not reach the companion NGC 4656 at the sensitivity level of the data. Spur 2 joins the disk over a large region of the major axis, at velocities which suggest it joins the outer galaxy. Spur 3 extends upwards from NGC 4631, but its base may not lie at the edge of the disk. One end of Spur 5 coincides in position and velocity with the top of Spur 3, and the other end lies to the north of Spur 1. No gas from the spurs can be firmly associated with the dwarf elliptical NGC 4627, although it shows signs of recent star formation, suggesting that it once contained gas.

(3) Emission far from the major axis of NGC 4631, and the generally disturbed appearance of the H I layer, is due mostly to outer disk phenomena: the inclination of the galaxy, the large scale-height in the outer galaxy, the connection of Spur 2 to the main disk, and features associated with Shell 1 and other spurs. If star formation is active in the outer galaxy, as the Hα morphology suggests, then it is difficult to distinguish gas raised off the plane by star formation from gas far from the major axis due to these other effects. High-latitude features associated with the inner disk are not absent, however, and these are likely to be due to star formation activity.

(4) The edge-on companion, NGC 4656, has a kinematic structure that suggests either very open spiral arms or a ring galaxy similar to the Cartwheel. High-latitude worms are present at velocities consistent with an outer disk origin. The most prominent worm stands above the center of the galaxy and forms a complete loop at marginal signal-to-noise ratios.

It is believed from observations at other wavelengths that an outflow from the disk exists in NGC 4631, although the outflow has not yet been searched for kinematically. The extended radio and X-ray halos, and the halo magnetic field vectors, which are better reproduced by a wind model than a dynamo model (Brandenburg et al. 1993), all point to the existence of an outflow. Given this evidence, one naturally expects that if star formation drives the outflow, it should be able to power a genuine high-z gaseous component. The fact that most of the H I far from the major axis has an outer disk origin does not rule out the possibility of star formation lifting much gas from the plane. The large modelled scale-height of the H I in the outer disk could be a consequence of star formation, although other causes such as flaring (in the relatively weak galactic potential) could also be at work. We suggested that star formation may be quite vigorous in the outer galaxy. If so, it becomes difficult to isolate high-z H I due to star formation from other causes. Fabry-Perot observations or long-slit spectra could reveal the distribution of star formation over the disk and test this suggestion.

Acknowledgements. Thanks go to the WSRT staff for carrying out the observations and calibration, and the GIPSY programmers for developing the new Unix-based package. E. Hummel is thanked for useful discussions about radio continuum emission from NGC 4631. Especially appreciated are the invaluable advice throughout this project and comments on the manuscript from R. Sancisi and J. M. van der Hulst.

References

Appleton P.N., Struck-Marcell C., 1987, ApJ 318, 103
Bosma A., 1981, AJ 86, 1791
Brandenburg A., Donner K.J., Moss D., et al., 1993, A&A 271, 36
Broeils A., 1993, PhD Thesis, University of Groningen
Burton, W.B., 1992, in: Pfenniger D., Bartholdi P. (eds) The galactic interstellar medium, (Berlin: Springer-Verlag) p. 1
Caldwell C.N., 1983, AJ 88, 804
Combes F., 1978, A&A 65, 47
Duric N., Crane P.C., Seaquist E.R., 1982, AJ 87, 1671
Fich M., Tremaine S., 1991, Ann. Rev. Astr. Ap. 29, 409
Ekers R.D., Sancisi R., 1977, A&A 54, 973
Gallouët L., Heidmann N., Dampierre F., 1973, A&AS 12, 89
Heiles C., 1984, ApJS 55, 585
van der Hulst J.M., et al, 1992, in: Worall D.M., Beimesderfer C., Barnes J. (eds.) Astronomical data analysis and software 1, ASP Conference Series vol. 25, p. 131
Hummel E., Dettmar R.-J., 1990, A&A 236, 33
Hummel E., Sancisi R., Ekers R.D., 1984, A&A 133, 1
Kamphuis J.J., 1993, PhD Thesis, University of Groningen
Kulkarni S.R., Heiles C., 1987, in: Hollenbach D.J., Thronson H.A. Jr. (eds.) Interstellar processes, Dordrecht: Reidel) p. 87
Rand R.J., van der Hulst J.M., 1993, AJ 105, 2098 (RH)
Rand R.J., Kulkarni S.R., Hester J.J., 1992, ApJ 396, 97 (RKH)
Rice W., Lonsdale C.J., et al., 1988, ApJS 68, 91
Roy J.-R., Wang J., Arsenault R., 1991, AJ 101, 825
Sandage A., 1961, The Hubble atlas of galaxies, Carnegie Institution of Washington
Spitzer L. Jr., 1978, Physical processes in the interstellar medium (John Wiley: New York)
de Vaucouleurs G., de Vaucouleurs A., et al., 1991, Third reference catalog of bright galaxies (Springer-Verlag)

Vigroux L., Lachieze Rey M., Souviron J., Vader J.P., 1985, in: Richter O.-G., Binggelli B. (eds.) ESO workshop on the Virgo cluster (ESO: Garching) p. 297

Walterbos R., 1993, in: Hollenbach D., Thronson H., Shull J.M. (eds.) The evolution of galaxies and their environment, p. 326

Weliachew L., Sancisi R., Guélin M., 1978, A&A 65, 37 (WSG)